2   Physical Properties of Marine Sediments

Monika Breitzke

Generally, physical properties of marine sediments are good indicators for the composition, microstructure and environmental conditions during and after the depositional process. Their study is of high interdisciplinary interest and follows various geoscientific objectives.

Physical properties provide a *lithological and geotechnical description* of the sediment. Questions concerning the composition of a depositional regime, slope stability or nature of seismic reflectors are of particular interest within this context. Parameters like P- and S-wave velocity and attenuation, elastic moduli, wet bulk density and porosity contribute to their solution.

As most physical properties can be measured very quickly in contrast to parameters like carbonate content, grain size distribution or oxygen isotope ratio, they often serve as *proxy parameters* for geological or paleoceanographical processes and changes in the environmental conditions. Basis for this approach are correlations between different parameters which allow to derive regression equations of regional validity. Highly resolved physical properties are used as input parameters for such equations to interpolate coarsely sampled geological, geochemical or sedimentological core logs. Examples are the P-wave velocity, attenuation and wet bulk density as indices for the sand content or mean grain size and the magnetic susceptibility as an indicator for the carbonate content or amount of terrigenous components. Additionally, highly resolved physical property core logs are often used for time series analysis to derive quaternary *stratigraphies* by orbital tuning.

In marine geochemistry, physical parameters which quantify the amount and distribution of pore space or indicate alterations due to diagenesis are important. Porosities are necessary to calculate flow rates, permeabilities describe how easy a fluid flows through a porous sediment and increased magnetic susceptibilities can be interpreted by an increased iron content or, more generally, by a high amount of magnetic particles within a certain volume.

This high interdisciplinary value of physical property measurements results from the different effects of changed environmental conditions on sediment structure and composition. Apart from anthropogeneous influences variations in the environmental conditions result from climatic changes and tectonic events which affect the ocean circulation and related production and deposition of biogenic and terrigenous components. Enhanced or reduced current intensities during glacial or interglacial stages cause winnowing, erosion and redeposition of fine-grained particles and directly modify the sediment composition. These effects are subject of sedimentological and paleoceanographical studies. Internal processes like early diagenesis, newly built authigenic sediments or any other alterations of the solid and fluid constituents of marine sediments are of geochemical interest. Gravitational mass transports at continental slopes or turbidites in large submarine fan systems deposit as coarse-grained chaotic or graded beddings. They can be identified in high-resolution physical property logs and are often directly correlated with sea level changes, results valuable for sedimentological, seismic and sequence stratigraphic investigations. Generally, any changes in the sediment structure which modify the elastic properties of the sediment influence the reflection characteristics of the subsurface and can be imaged by remote sensing seismic or echosounder surveys.
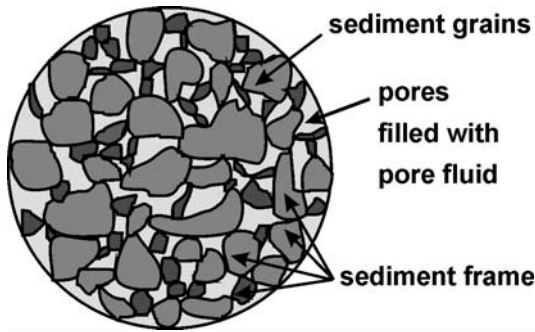
Fig. 2.1 Components of marine sediments. The single particles are the sediment grains. The voids between these particles – the pores – are filled with pore fluid, usually sea water. Welded particles and sediment grains in close contact build the sediment frame.

2.1   Introduction

Physical properties of marine sediments depend on the properties and arrangement of the solid and fluid constituents. To fully understand the image of geological and paleoceanographical processes in physical property core logs it is helpful to consider the single components in detail (Fig. 2.1).

By most general definition a sediment is a collection of particles - the sediment grains - which are loosely deposited on the sea floor and closely packed and consolidated under increasing lithostatic pressure. The voids between the sediment grains - the pores - form the pore space. In water-saturated sediments it is filled with pore water. Grains in close contact and welded particles build the sediment frame. Shape, arrangement, grain size distribution and packing of particles determine the elasticity of the frame and the relative amount of pore space.

Measurements of physical properties usually encompass the whole, undisturbed sediment. Two types of parameters can be distinguished: (1) bulk parameters and (2) acoustic and elastic parameters. Bulk parameters only depend on the relative amount of solid and fluid components within a defined sample volume. They can be approximated by a simple volume-oriented model (Fig. 2.2a). Examples are the wet bulk density and porosity. In contrast, acoustic and elastic parameters depend on the relative amount of solid and fluid components and on the sediment frame including arrangement, shape and grain size distribution of the solid particles. Viscoelastic wave propagation models simulate these complicated structures, take the elasticity of the frame into account and consider interactions between solid and fluid constituents. (Fig. 2.2b). Examples are the velocity and attenuation of P- and S-waves. Closely related parameters which mainly depend on the distribution and capillarity of the pore space are the permeability and electrical resistivity.

Various methods exist to measure the different physical properties of marine sediments. Some parameters can be measured directly, others
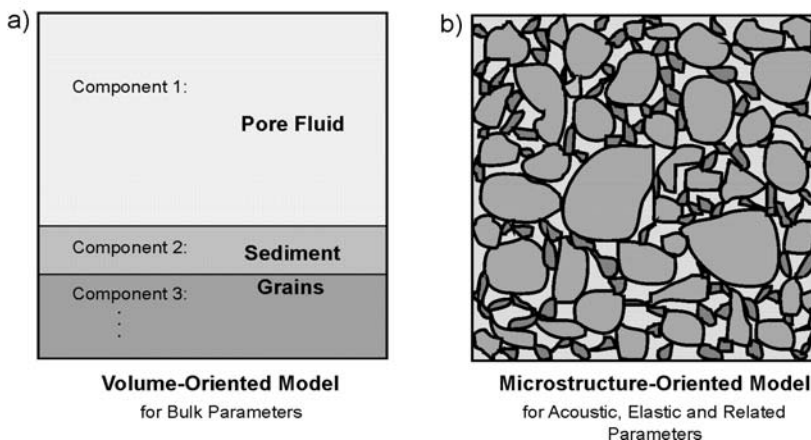
Fig. 2.2 Two types of sediment models. (a) The layered, volume-oriented model for bulk parameters only depends on the relative amount of solid and fluid components. (b) The microstructure-oriented model for acoustic and elastic parameters takes the complicated shape and geometry of the particle and pore size distribution into account and considers interactions between the solid and fluid constituents during wave propagation.

indirectly by determining one or several related parameters and computing the desired property by empirical or model-based equations. For consolidated sedimentary, igneous and metamorphic rocks Schön (1996) described a large variety of such methods for all common physical properties. Some of these methods can also be applied to unconsolidated, water-saturated sediments, others have to be modified or are completely inappropriate. Principally, if empirical relations or sediment models are used, the implicit assumptions have to be checked carefully. An example is Archie's law (Archie 1942) which combines the electrical resistivities of the pore fluid and saturated sediment and with its porosity. An exponent and multiplier in this equation depend on the sediment type and composition and change from fine- to coarse-grained and from terrigenous to biogenic sediments. Another example is Wood's equation (Wood 1946) which relates P-wave velocities to porosities. This model approximates the sediment by a dilute suspension and neglects the sediment frame, any interactions between particles or particles and pore fluid and assumes a 'zero' frequency for acoustic measurements. Such assumptions are only valid for a very limited set of high porosity sediments so that for any comparisons these limitations should be kept in mind.

Traditional measuring techniques use small chunk samples taken from the split core. These techniques are rather time-consuming and could only be applied at coarse sampling intervals. The necessity to measure high-resolution physical property logs rapidly on a milli- to centimeter scale for a core-to-core or core-to-seismic data correlation, and the opportunity to use high-resolution physical property logs for stratigraphic purposes (e.g. orbital tuning) forced the development of non-destructive, automated logging systems. They record one or several physical properties almost continuously at arbitrary small increments under laboratory conditions. The most common tools are the multi sensor track (MST) system for P-wave velocity, wet bulk density and magnetic susceptibility core logging onboard of the *Ocean Drilling Program* research vessel JOIDES Resolution (e.g. Shipboard Scientific Party 1995), and the commercially available multi sensor core logger (MSCL) of GEOTEK™ (Schultheiss and McPhail 1989; Weaver and Schultheiss 1990; Gunn and Best 1998). Additionally, other core logging tools have simultaneously been developed for special research

interests which for instance record electrical resistivities (Bergmann 1996) or full waveform transmission seismograms on sediment cores (Breitzke and Spieß 1993). They are particularly discussed in this paper.

While studies on sediment cores only provide information on the local core position, lateral variations in physical properties can be imaged by remote sensing methods like high-resolution seismic or sediment echosounder profiling. They facilitate core-to-core correlations over large distances and allow to evaluate physical property logs within the local sedimentation environment.

In what follows the theoretical background of the most common physical properties and their measuring tools are described. Examples for the wet bulk density and porosity can be found in Section 2.2. For the acoustic and elastic parameters first the main aspects of Biot-Stoll's viscoelastic model which computes P- and S-wave velocities and attenuations for given sediment parameters (Biot 1956a, b, Stoll 1974, 1977, 1989) are summarized. Subsequently, analysis methods are described to derive these parameters from transmission seismograms recorded on sediment cores, to compute additional properties like elastic moduli and to derive the permeability as a related parameter by an inversion scheme (Sect. 2.4).

Examples from terrigenous and biogenic sedimentation provinces are presented (1) to illustrate the large variability of physical properties in different sediment types and (2) to establish a sediment classification which is only based on physical properties, in contrast to geological sediment classifications which mainly uses parameters like grain size distribution or mineralogical composition (Sect. 2.5).

Finally, some examples from high-resolution narrow-beam echosounder recordings present remote sensing images of terrigenous and biogenic sedimentation environments (Sect. 2.6).

2.2   Porosity and Wet Bulk Density

Porosity and wet bulk density are typical bulk parameters which are directly associated with the relative amount of solid and fluid components in marine sediments. After definition of both parameters this section first describes their traditional analysis method and then focuses on recently developed techniques which determine porosities

and wet bulk densities by gamma ray attenuation and electrical resistivity measurements.

The porosity (ϕ) characterizes the relative amount of pore space within a sample volume. It is defined by the ratio

$$\phi = \frac{volume\ of\ pore\ space}{total\ sample\ volume} = \frac{V_f}{V} \qquad (2.1)$$

Equation 2.1 describes the fractional porosity which ranges from 0 in case of none pore volume to 1 in case of a water sample. Multiplication with 100 gives the porosity in percent. Depending on the sediment type porosity occurs as *inter-* and *intraporosity*. Interporosity specifies the pore space between the sediment grains and is typical for terrigenous sediments. Intraporosity includes the voids within hollow sediment particles like foraminifera in calcareous ooze. In such sediments both inter- and intraporosity contribute to the total porosity.

The wet bulk density (ρ) is defined by the mass (m) of a water-saturated sample per sample volume (V)

$$\rho = \frac{mass\ of\ wet\ sample}{total\ sample\ volume} = \frac{m}{V} \qquad (2.2)$$

Porosity and wet bulk density are closely related, and often porosity values are derived from wet bulk density measurements and vice versa. Basic assumption for this approach is a two-component model for the sediment with uniform grain and pore fluid densities (ρ_g) and (ρ_f). The wet bulk density can then be calculated using the porosity as a weighing factor

$$\rho = \phi \cdot \rho_f + (1 - \phi) \cdot \rho_g \qquad (2.3)$$

If two or several mineral components with significantly different grain densities contribute to the sediment frame their densities are averaged in (ρ_g).

2.2.1   Analysis by Weight and Volume

The traditional way to determine porosity and wet bulk density is based on weight and volume measurements of small sediment samples. Usually they are taken from the centre of a split core by a syringe which has the end cut off and a definite volume of e.g. 10 ml. While weighing can be done very accurately in shore-based laboratories mea-

surements onboard of research vessels require special balance systems which compensate the shipboard motions (Childress and Mickel 1980). Volumes are measured precisely by Helium gas pycnometers. They mainly consist of a sample cell and a reference cell and employ the ideal gas law to determine the sample volume. In detail, the sediment sample is placed in the sample cell, and both cells are filled with Helium gas. After a valve connecting both cells are closed, the sample cell is pressurized to (P_1). When the valve is opened the pressure drops to (P_2) due to the increased cell volume. The sample volume (V) is calculated from the pressure ratio (P_1/P_2) and the volumes of the sample and reference cell, (V_s) and (V_{ref}) (Blum 1997).

$$V = V_s + \frac{V_{ref}}{1 - P_1/P_2} \qquad (2.4)$$

While weights are measured on wet and dry samples having used an oven or freeze drying, volumes are preferentially determined on dry samples. A correction for the mass and volume of the salt precipitated from the pore water during drying must additionally be applied (Hamilton 1971; Gealy 1971) so that the total sample volume (V) consists of

$$V = V_{dry} - V_{salt} + V_f \qquad (2.5)$$

The volumes (V_f) and (V_{salt}) of the pore space and salt result from the masses of the wet and dry sample, (m) and (m_{dry}), from the densities of the pore fluid and salt ($\rho_f = 1.024$ g cm^{-3} and $\rho_{salt} = 2.1$ g cm^{-3}) and from the fractional salinity (s)

$$V_f = \frac{m_f}{\rho_f} = \frac{m - m_{dry}}{(1 - s) \cdot \rho_f} \qquad (2.6)$$

$$\text{with}: \qquad m_f = \frac{m - m_{dry}}{1 - s}$$

$$V_{salt} = \frac{m_{salt}}{\rho_{salt}} = \frac{m_f - (m - m_{dry})}{\rho_{salt}} \qquad (2.7)$$

$$\text{with}: \qquad m_{salt} = m_f - (m - m_{dry})$$

Together with the mass (m) of the wet sample equations 2.5 to 2.7 allow to compute the wet bulk density according to equation 2.2.

Wet bulk density computations according to equation 2.3 require the knowledge of grain

densities (ρ_g). They can also be determined from weight and volume measurements on wet and dry samples (Blum 1997)

$$\rho_g = \frac{m_g}{V_g} = \frac{m_{dry} - m_{salt}}{V_{dry} - V_{salt}} \qquad (2.8)$$

Porosities are finally computed from the volumes of the pore space and sample as defined by the equations above.

2.2.2   Gamma Ray Attenuation

The attenuation of gamma rays passing radially through a sediment core is a widely used effect to analyze wet bulk densities and porosities by a non-destructive technique. Often ^{137}Cs is used as source which emits gamma rays of 662 keV energy. They are mainly attenuated by Compton scattering (Ellis 1987). The intensity I of the attenuated gamma ray beam depends on the source intensity (I_0), the wet bulk density (ρ) of the sediment, the ray path length (d) and the specific Compton mass attenuation coefficient (μ)

$$I = I_0 \cdot e^{-\mu \rho d} \qquad (2.9)$$

To determine the source intensity in practice and to correct for the attenuation in the liner walls first no core and then an empty core liner are placed between the gamma ray source and detector to measure the intensities (I_{air}) and (I_{liner}). The difference ($I_{air} - I_{liner}$) replaces the source intensity (I_0), and the ray path length (d) is substituted by the measured outer core diameter ($d_{outside}$) minus the double liner wall thickness ($2d_{liner}$). With these corrections the wet bulk density (ρ) can be computed according to

$$\rho = -\frac{1}{\mu \cdot (d_{outside} - 2d_{liner})} \cdot \ln\left(\frac{I}{I_{air} - I_{liner}}\right) \qquad (2.10)$$

Porosities are derived by rearranging equation 2.3 and assuming a grain density (ρ_g).

The specific Compton mass attenuation coefficient (μ) is a material constant. It depends on the energy of the gamma rays and on the ratio (Z/A) of the number of electrons (Z) to the atomic mass (A) of the material (Ellis 1987). For most sediment and rock forming minerals this ratio is about 0.5, and for a ^{137}Cs source the corresponding mass attenuation coefficient (μ_g) for sediment grains is 0.0774 cm^2 g^{-1}. However, for the hydro-

gen atom (Z/A) is close to 1.0 leading to a significantly different mass attenuation coefficient (μ_f) in sea water of 0.0850 cm^2 g^{-1} (Gerland and Villinger 1995). So, in water-saturated sediments the effective mass attenuation coefficient (μ) results from the sum of the mass weighted coefficients of the solid and fluid constituents (Bodwadkar and Reis 1994)

$$\mu = \phi \cdot \frac{\rho_f}{\rho} \cdot \mu_f + (1 - \phi) \cdot \frac{\rho_g}{\rho} \cdot \mu_g \qquad (2.11)$$

The wet bulk density (ρ) in the denominator is defined by equation 2.3. Unfortunately, equations 2.3 and 2.11 depend on the porosity (ϕ), a parameter which should actually be determined by gamma ray attenuation. Gerland (1993) used an average 'processing porosity' of 50% for terrigenous, 70% for biogenic and 60% for cores of mixed material to estimate the effective mass attenuation coefficient for a known grain density. Whitmarsh (1971) suggested an iterative scheme which improves the mass attenuation coefficient. It starts with an estimated 'processing porosity' and mass attenuation coefficient (eq. 2.11) to calculate the wet bulk density from the measured gamma ray intensity (eq. 2.10). Subsequently, an improved porosity (eq. 2.3) and mass attenuation coefficient (eq. 2.11) can be calculated for a given grain density. Using these optimized values in a second iteration wet bulk density, porosity and mass attenuation coefficient are re-evaluated. Gerland (1993) and Weber et al. (1997) showed that after few iterations (< 5) the values of two successive steps differ by less than 0.1‰ even if a 'processing porosity' of 0 or 100% and a mass attenuation coefficient of 0.0774 cm^2 g^{-1} or 0.0850 cm^2 g^{-1} for a purely solid or fluid 'sediment' are used as starting values.

Gamma ray attenuation is usually measured by automated logging systems, e.g. onboard of the *Ocean Drilling Program* research vessel JOIDES Resolution (Boyce 1973, 1976) by the multisensor core logger of GEOTEK™ (Schultheiss and McPhail 1989; Weaver and Schultheiss 1990; Gunn and Best 1998) or by specially developed systems (Gerland 1993; Bodwadkar and Reis 1994; Gerland and Villinger 1995). The emission of gamma rays is a random process which is quantified in counts per second, and which are converted to wet bulk densities by appropriate calibration curves (Weber et al. 1997). To get a representative value

for the gamma ray attenuation gamma counts must be integrated over a sufficiently long time interval. How different integration times and measuring increments influence the quality, resolution and reproducibility of gamma ray logs illustrates Figure 2.3. A 1 m long section of gravity core PS2557-1 from the South African continental margin was repeatedly measured with increments from 1 to 0.2 cm and integration times from 10 to 120 s. Generally, the dominant features, which can be related to changes in the lithology, are reproduced in all core logs. The prominent peaks are more pronounced and have higher amplitudes if the integration time increases (from A to D). Additionally, longer integration times reduce the scatter (from A to B). Fine-scale lithological variations are best resolved by the shortest measuring increment (D).
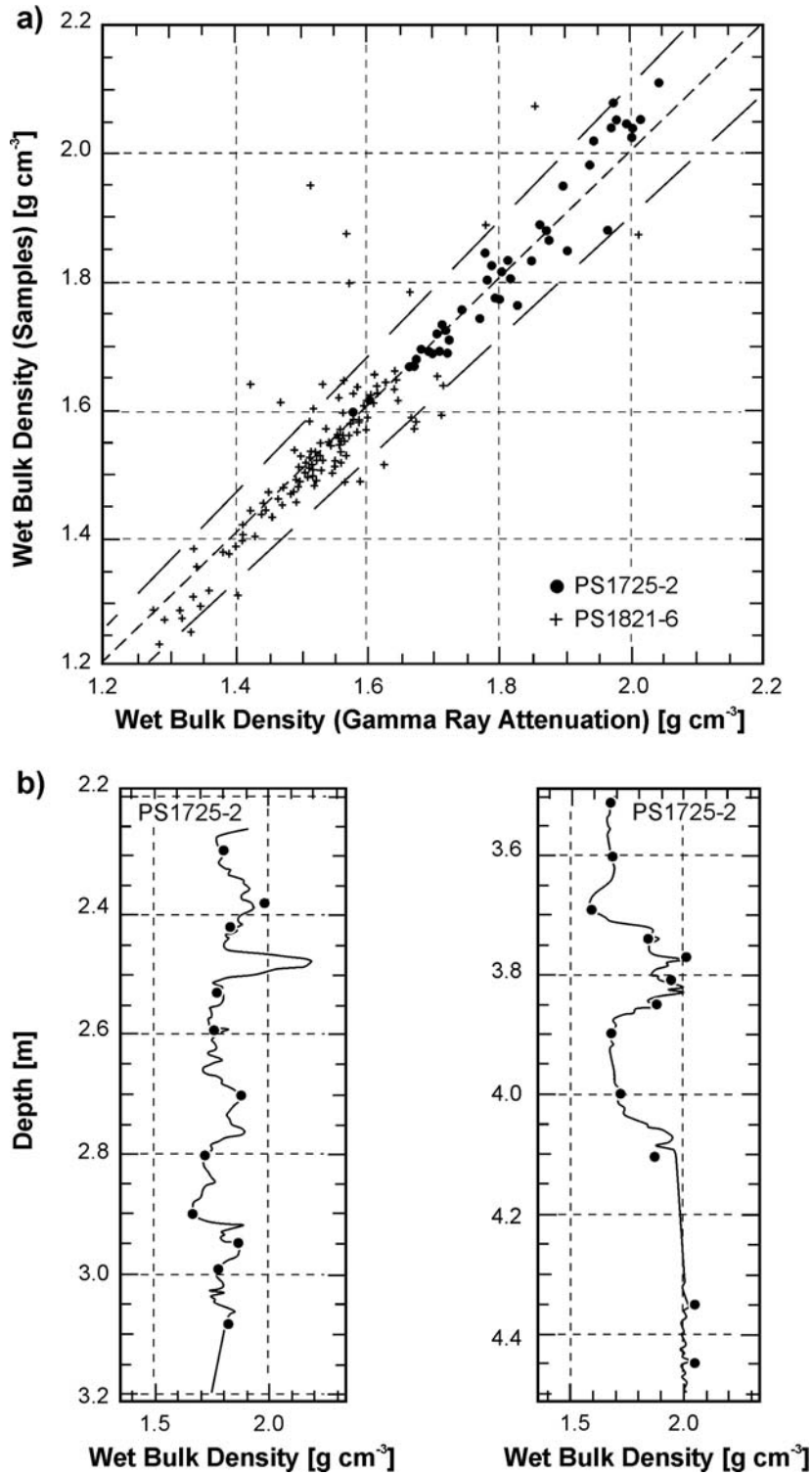
A comparison of wet bulk densities derived from gamma ray attenuation with those measured on discrete samples is shown in Figure 2.4a for two gravity cores from the Arctic (PS1725-2) and Antarctic Ocean (PS1821-6). Wet bulk densities,

porosities and grain densities of the discrete samples were analyzed by their weight and volume. These grain densities and a constant 'processing porosity' of 50% were used to evaluate the gamma counts. Displayed versus each other both data sets essentially differ by less than ±5% (dashed lines). The lower density range (1.20 - 1.65 g cm^{-3}) is mainly covered by the data of the diatomaceous and terrigenous sediments of core PS1821-6 while the higher densities (1.65 - 2.10 g cm^{-3}) are characteristic for the terrigenous core PS1725-2. According to Gerland and Villinger (1995) the scatter in the correlation of both data sets probably results from (1) a slight shift in the depth scales, (2) the fact that both measurements do not consider identical samples volumes, and (3) artefacts like drainage of sandy layers due to core handling, transportation and storage.

A detailed comparison of both data sets is shown in Figure 2.4b for two segments of core PS1725-2. Wet bulk densities measured on discrete samples agree very well with the density log derived from gamma ray attenuation. Additionally,
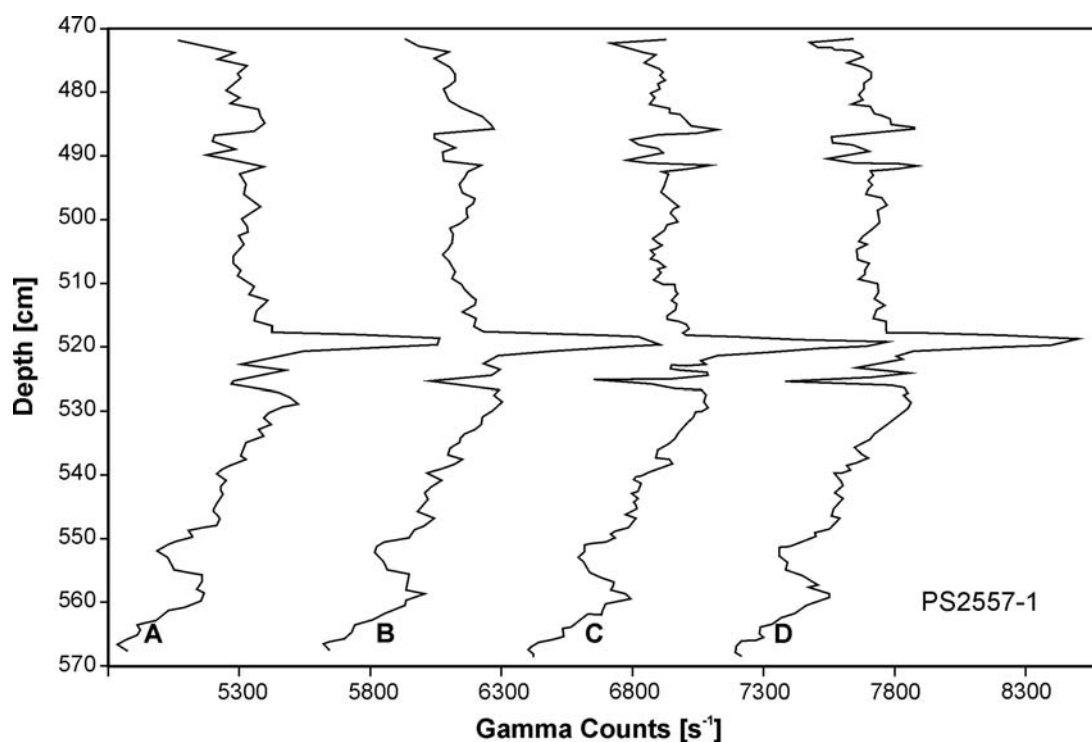
Fig. 2.3 Gamma counts for a 1 m long core section of gravity core PS2557-1 used to illustrate the influence of various integration times and measuring increments. Curve A is recorded with an increment of 1 cm and an integration time of 10 s, curve B with an increment of 1 cm and an integration time of 20 s, curve C with an increment of 0.5 cm and an integration time of 60 s and curve D with an increment of 0.2 cm and an integration time of 120 s. To facilitate the comparison each curve is set off by 800 counts. Modified after Weber et al. (1997).

Fig. 2.4 Comparison of wet bulk densities determined on discrete samples by weight and volume measurements and calculated from gamma ray attenuation. (a) Cross plot of wet bulk densities of gravity cores PS1821-6 from the Antarctic and PS1725-2 from the Arctic Ocean. The dashed lines indicate a difference of ±5% between both data sets. (b) Wet bulk density logs derived from gamma ray attenuation for two 1 m long core sections of gravity core PS1725-2. Superimposed are density values measured on discrete samples. Modified after Gerland and Villinger (1995).

the striking advantage of the almost continuous wet bulk density log clearly becomes obvious. Measured with an increment of 5 mm a lot of fine-scale variations are defined, a resolution which could never be reached by the time-consuming analysis of discrete samples (Gerland 1993; Gerland and Villinger 1995).

The precision of wet bulk densities can be slightly improved, if the iterative scheme for the mass attenuation coefficient is applied (Fig. 2.5a). For core PS1725-2 wet bulk densities computed with a constant mass attenuation coefficient are compared with those derived from the iterative procedure. Below 1.9 g cm^{-3} the iteration produces slightly smaller densities than are determined with a constant mass attenuation coefficient and are

thus below the dotted 1:1 line. Above 1.9 g cm^{-3} densities based on the iterative procedure are slightly higher.

If both data sets are plotted versus the wet bulk densities of the discrete samples the optimization essentially becomes obvious for high densities (>2.0 g cm^{-3}, Fig. 2.5b). After iteration densities are slightly closer to the dotted 1:1 line.

While this improvement is usually small and here only on the order of 1.3% ($\approx$0.02 g cm^{-3}), differences between assumed and true grain density affect the iteration more distinctly (Fig. 2.5c). As an example wet bulk densities of core PS1725-2 were calculated with constant grain densities of 2.65, 2.75 and 2.10 g cm^{-3}, values which are typical for calcareous, terrigenous and diatomaceous
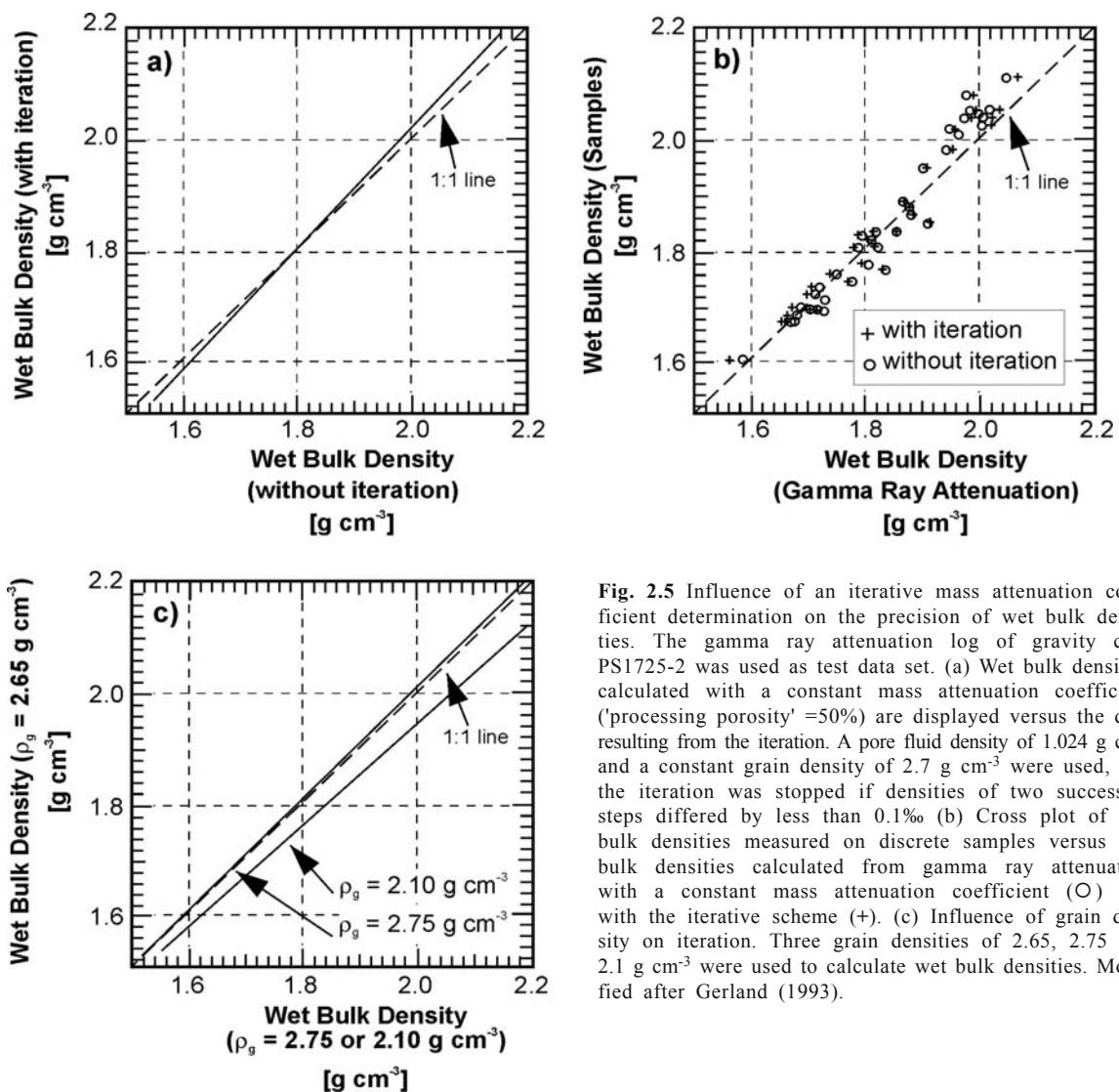
Fig. 2.5 Influence of an iterative mass attenuation coefficient determination on the precision of wet bulk densities. The gamma ray attenuation log of gravity core PS1725-2 was used as test data set. (a) Wet bulk densities calculated with a constant mass attenuation coefficient ('processing porosity' =50%) are displayed versus the data resulting from the iteration. A pore fluid density of 1.024 g cm^{-3} and a constant grain density of 2.7 g cm^{-3} were used, and the iteration was stopped if densities of two successive steps differed by less than 0.1‰ (b) Cross plot of wet bulk densities measured on discrete samples versus wet bulk densities calculated from gamma ray attenuation with a constant mass attenuation coefficient (○) and with the iterative scheme (+). (c) Influence of grain density on iteration. Three grain densities of 2.65, 2.75 and 2.1 g cm^{-3} were used to calculate wet bulk densities. Modified after Gerland (1993).

sediments. Displayed as cross-plot, calculations with grain densities of 2.65 and 2.75 g cm^{-3} almost coincide and follow the dotted 1:1 line. However, computations with a grain density of 2.10 g cm^{-3} differ by 1.3 - 3.6% (0.02 - 0.08 g cm^{-3}) from those with a grain density of 2.65 g cm^{-3}. This result is particularly important for cores composed of terrigenous and biogenic material of significantly different grain densities like the terrigenous and diatomaceous components in core PS1821-6. Here, an iteration with a constant grain density of 2.65 g cm^{-3} would give erroneous wet bulk densities in the diatomaceous parts. In such cores a depthdependent grain density profile should be applied in combination with the iterative procedure, or otherwise wet bulk densities would better be calculated with a constant mass attenuation coefficient. However, if the grain density is almost constant downcore the iterative scheme could be applied without any problems.

2.2.3 Electrical Resistivity (Galvanic Method)

The electrical resistivity of water-saturated sediments depends on the resistivity of its solid and fluid constituents. However, as the sediment grains are poor conductors an electrical current mainly propagates in the pore fluid. The dominant transport mechanism is an electrolytic conduction by ions and molecules with an excess or deficiency of electrons. Hence, current propagation in water-saturated sediments actually transports material through the pore space, so that the resistivity depends on both the conductivity of the pore water and the microstructure of the sediment. The conductivity of pore water varies with its salinity, and mobility and concentration of dissolved ions and molecules. The microstructure of the sediment is controlled by the amount and distribution of pore space and its capillarity and tortuosity. Thus, the electrical resistivity cannot be considered as a bulk parameter which strictly only depends on the relative amount of solid and fluid components, but as shown below, it can be used to derive porosity and wet bulk density as bulk parameters after calibration to a 'typical' sediment composition of a local sedimentation environment.

Several models were developed to describe current flow in rocks and water-saturated sediments theoretically. They encompass simple plane layered models (Waxman and Smits 1968) as well as complex approximations of pore space by self similar models (Sen et al. 1981), effective medium theories (Sheng 1991) and fractal geometries (Ruffet et al. 1991). In practice these models are of minor importance because often only few of the required model parameters are known. Here, an empirical equation is preferred which relates the resistivity (R_s) of the wet sediment to its fractional porosity (ϕ) (Archie 1942)

$$F = \frac{R_s}{R_f} = a \cdot \phi^{-m} \qquad (2.12)$$

The ratio of the resistivity (R_s) in sediment to the resistivity (R_f) in pore water defines the formation (resistivity) factor (F). (a) and (m) are constants which characterize the sediment composition. As Archie (1942) assumed that (m) indicates the consolidation of the sediment it is also called cementation exponent (cf. Sect. 3.2.2). Several authors derived different values for (a) and (m). For an overview please refer to Schön (1996). In marine sediments often Boyce's (1968) values (a = 1.3, m = 1.45), determined by studies on diatomaceous, silty to sandy arctic sediments, are applied. Nevertheless, these values can only be rough estimates. For absolutely correct porosities both constants must be calibrated by an additional porosity measurement, either on discrete samples or by gamma ray attenuation. Such calibrations are strictly only valid for that specific data set but, with little loss of accuracy, can be transferred to regional environments with similar sediment compositions. Wet bulk densities can then be calculated using equation 2.3 and assuming a grain density (cf. also section 3.2.2).

Electrical resistivities can be measured on split cores by a half-automated logging system (Bergmann 1996). It measures the resistivity (R_s) and temperature (T) by a small probe which is manually inserted into the upper few millimeters of the sediment. The resistivity (R_f) of the interstitial pore water is simultaneously calculated from a calibration curve which defines the temperature-conductivity relation of standard sea water (35‰ salinity) by a fourth power law (Siedler and Peters 1986).

The accuracy and resolution that can be achieved compared to measurements on discrete samples were studied on the terrigenous square barrel kastenlot core PS2178-5 from the Arctic Ocean. If both data sets are displayed as cross plots porosities mainly range within the dashed 10% error lines, while densities mainly differ by
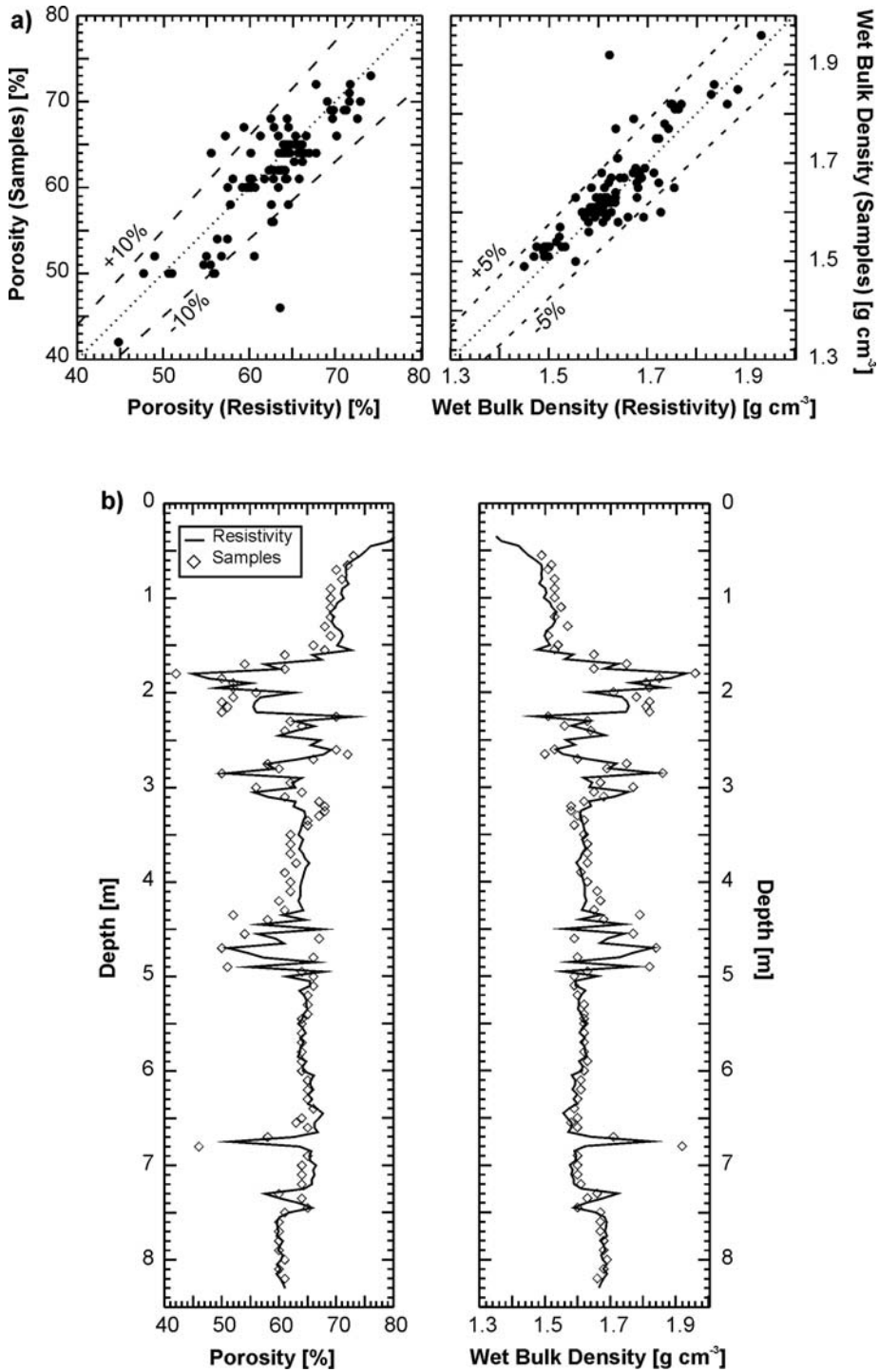
Fig. 2.6 Comparison of porosities and wet bulk densities measured on discrete samples and by electrical resistivities. Boyce's (1968) values for the coefficients (a) and (m) and pore fluid and grain densities of 1.024 g cm⁻³ and 2.67 g cm⁻³ were used to convert formation factors into porosities and wet bulk densities. Wet and dry weights and volumes were analyzed on discrete samples. (a) Cross plots of both data sets for square barrel kastenlot core PS2178-5. The dashed lines indicate an error of 10% for the porosity and 5% for the density data. (b) Porosity and wet bulk density logs of core PS2178-5 derived from resistivity measurements. Superimposed are porosity and density values measured on discrete samples. Data from Bergmann (1996).
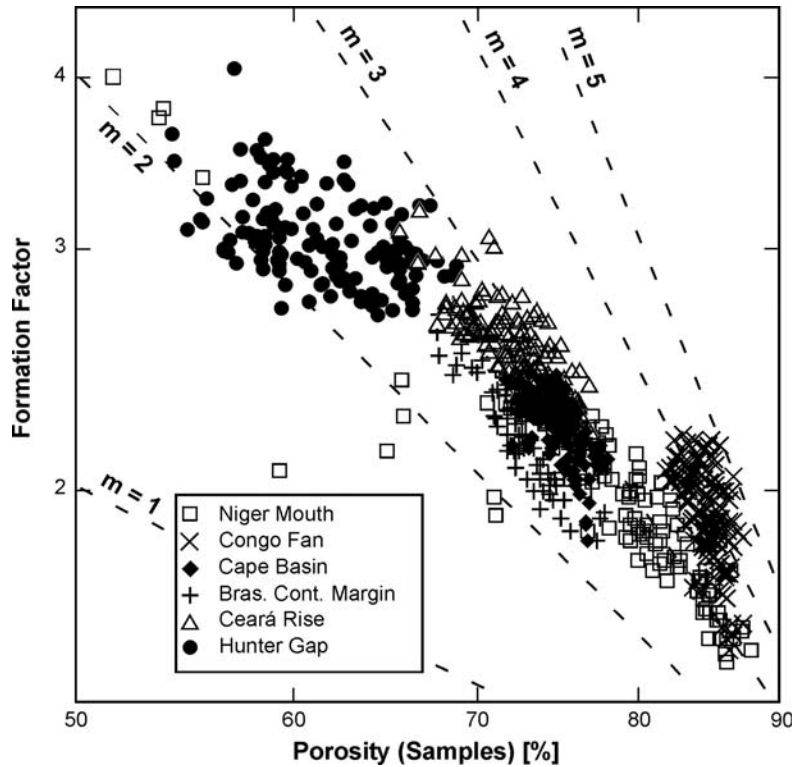
Fig. 2.7 Formation factor versus porosity for six gravity cores retrieved from different sedimentation provinces in the South Atlantic. Porosities were determined on discrete samples by wet and dry weights and volumes, formation factors by resistivity measurements. The dashed lines indicate Archie's law for a = 1 and cementation exponents (m) between 1 and 5. For a description of the sedimentation provinces, core numbers, coring locations, sediment compositions, water depths and constants (a) and (m) derived from linear least square fits please refer to Table 2.1. Unpublished data from M. Richter, University Bremen, Germany.

less than 5% (Fig. 2.6a). The core logs illustrate that the largest differences occur in the laminated sandy layers, particularly between 1.5 and 3.5 m and between 4.3 and 5.1 m depth (Fig. 2.6b). A drainage of the sandy layers, slight differences in the depth scale and different volumes considered by both methods probably cause this scatter. Nevertheless, in general both data sets agree very well having used Boyce's (1968) values for (a) and (m) and a typical terrigenous grain density of 2.67 g/cm³ for porosity and wet bulk density computations. This is valid because the sedimentation environment of core PS2178-5 from the Arctic Ocean is rather similar to the Bering Sea studied by Boyce (1968).

The influence of the sediment composition on the formation factor-porosity relation illustrates Figure 2.7 for six provinces in the South Atlantic. For each core porosities and formation factors were evaluated at the same core depths by wet and dry weights and volumes of discrete samples

and by electrical resistivities. Displayed as a cross plot on a log-log scale the data sets of each core show different trends and thus different cementation exponents. Jackson et al. (1978) tried to relate such variations in the cementation exponent to the sphericity of sediment particles. Based on studies on artificial samples they found higher cementation exponents if particles become less spherical. For natural sediments incorporating a large variety of terrigenous and biogenic particle sizes and shapes, it is difficult to verify similar relations. It is only obvious that coarse-grained calcareous foraminiferal oozes from the Hunter Gap show the lowest and fine-grained, diatom-bearing hemipelagic mud from the Congo Fan upwelling the highest cementation exponent. Simultaneously, the constant (a) decreases with increasing cementation exponent (Tab. 2.1). Possibly, in natural sediments the amount and distribution of pore space are more important than the particle shape. Generally, cementation exponent (m),

constant (a) and formation factor (F) together characterize a specific environment. Table 2.1 summarizes the values of (a) and (m) derived from a linear least square fit to the log-log display of the data sets and shortly describes the sediment compositions.

With these values for (a) and (m) calibrated porosity logs are calculated which agree well with porosities determined on discrete samples (Fig. 2.8, black curves). The error in porosity that may result from using the 'standard' Boyce's (1968) values for (a) and (m) instead of those derived from the calibration appears in two different ways (gray curves). (1) The amplitude of the downcore porosity variations might be too large, as is illustrated by core GeoB2110-4 from the Brazilian Continental Margin. (2) The log might be shifted to higher or lower porosities, as is shown by core GeoB1517-1 from the Ceará Rise. Only if linear regression results in values for (a) and (m) close to Boyce's (1968) coefficients the error in the porosity log is negligible (core GeoB1701-4 from the Niger Mouth).

In order to compute absolutely correct wet bulk densities from calibrated porosity logs a grain density must be assumed. For most terrigenous and calcareous sediment cores this parameter is not very critical as it often only changes by few percent downcore (e.g. 2.6 - 2.7 g cm^{-3}). However, in cores from the Antarctic Polar Frontal Zone where an interlayering of diatomaceous and calcareous oozes indicates the advance and retreat of the oceanic front during glacial and interglacial stages grain densities may vary between about 2.0 and 2.8 g cm^{-3}. Here, depth-dependent values must either be known or modeled in order to get correct wet bulk density variations from resistivity measurements. An example for this approach are resistivity measurements on ODP core 690C from the Maud Rise (Fig. 2.9). While the carbonate log (b) clearly indicates calcareous layers with high and diatomaceous layers with zero CaCO$_3$ percentages (O'Connell 1990), the resistivity-based porosity log (a) only scarcely reflects these lithological changes. The reason is that calcareous and diatomaceous oozes are characterized by high inter- and intraporosities incorporated in and between hollow foraminifera and diatom shells. In contrast, the wet bulk density log measured onboard of JOIDES Resolution by gamma ray attenuation ((c), gray curve) reveals pronounced variations. They obviously correlate with the CaCO$_3$-content and can thus only be attributed to downcore changes in the grain density. So, a grain density model (d) was developed. It averages the densities of carbonate (ρ_{carb} = 2.8 g cm^{-3}) and biogenic opal (ρ_{opal} = 2.0 g cm^{-3}) (Barker, Kennnett et al. 1990) according to the fractional CaCO$_3$-content (C), $\rho_{model} = C \times \rho_{carb} + (1 - C) \times \rho_{opal}$. Based on this model wet bulk densities ((c), black curve) were derived from

Table 2.1 Geographical coordinates, water depth, core length, region and composition of the sediment cores considered in Figure 2.7. The cementation exponent (m) and the constant (a) are derived from the slope and intercept of a linear least square fit to the log-log display of formation factors versus porosities.

| Core	Coordinates	Water Depth	Core Length	Region	Sediment Composition	Factor (a)	Cementation Exponent (m)
GeoB 1306-2	35°12.4'S 26°45.8'W	4058 m	6.97 m	Hunter Gap	foram.-nannofossil ooze, sandy	1,6	1,3
GeoB 1517-1	04°44.2'N 43°02.8'W	4001 m	6.89 m	Ceará Rise	nannofossil-foram. ooze	1,3	2,1
GeoB 1701-4	01°57.0'N 03°33.1'E	4162 m	7.92 m	Niger Mouth	clayey mud, foram. bearing	1,4	1,4
GeoB 1724-2	29°58.2'S 08°02.3'E	5084 m	7.45 m	Cape Basin	red clay	1,0	2,8
GeoB 2110-4	28°38.8'S 45°31.1'W	3011 m	8.41 m	Braz. Cont. Margin	pelagic clay. Foram. bearing	0,8	3,3
GeoB 2302-2	05°06.4'S 10°05.5'E	1830 m	14.18 m	Congo Fan	hemipelagic mud, diatom bearing, H$_2$S	0,8	5,3

the porosity log which agree well with the gamma ray attenuation densities ((c), gray curve) and show less scatter.

Though resistivities are only measured half-automatically including a manual insertion and removal of the probe, increments of 1 - 2 cm can be realized within an acceptable time so that more fine-scale structures can be resolved than by analysis of discrete samples. However, the real advantage compared to an automated gamma ray attenuation logging is that the resistivity measurement system can easily be transported, e.g.

onboard of research vessels or to core repositories, while the transport of radioactive sources requires special safety precautions.

2.2.4 Electrical Resistivity (Inductive Method)

A second, non-destructive technique to determine porosities by resistivity measurements uses a coil as sensor. A current flowing through the coil induces an electric field in the unsplit sediment core while it is automatically transported through
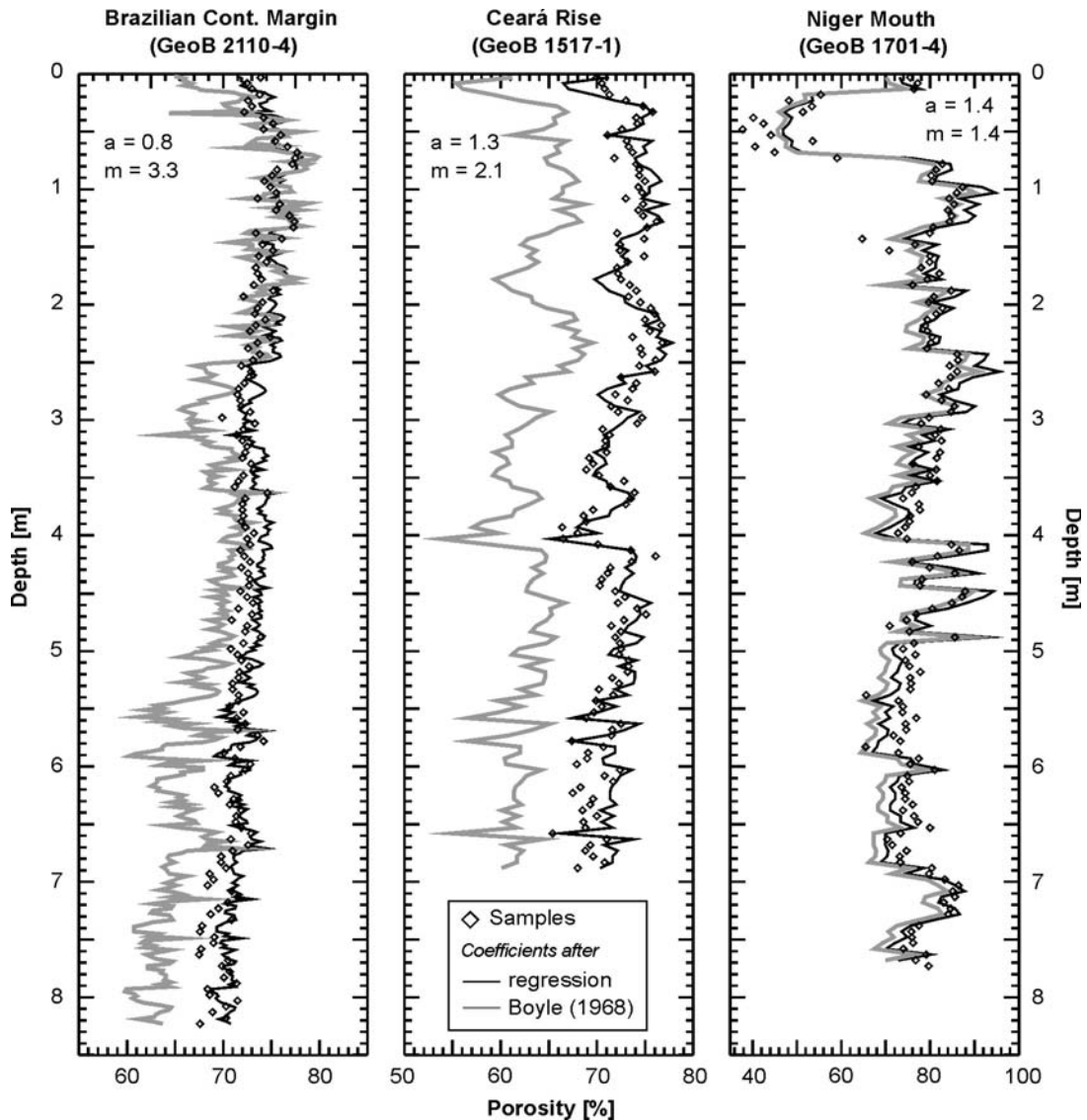
Fig. 2.8 Porosity logs determined by resistivity measurements on three gravity cores from the South Atlantic (see also Fig. 2.7 and Table 2.1). Gray curve: Boyce's (1968) values were used for the constants (a) and (m). Black curve: (a) and (m) were derived from the slope and intercept of a linear least square fit. These values are given at the top of each log. Superimposed are porosities determined on discrete samples by weight and volume measurements (unpublished data from P. Müller, University Bremen, Germany).
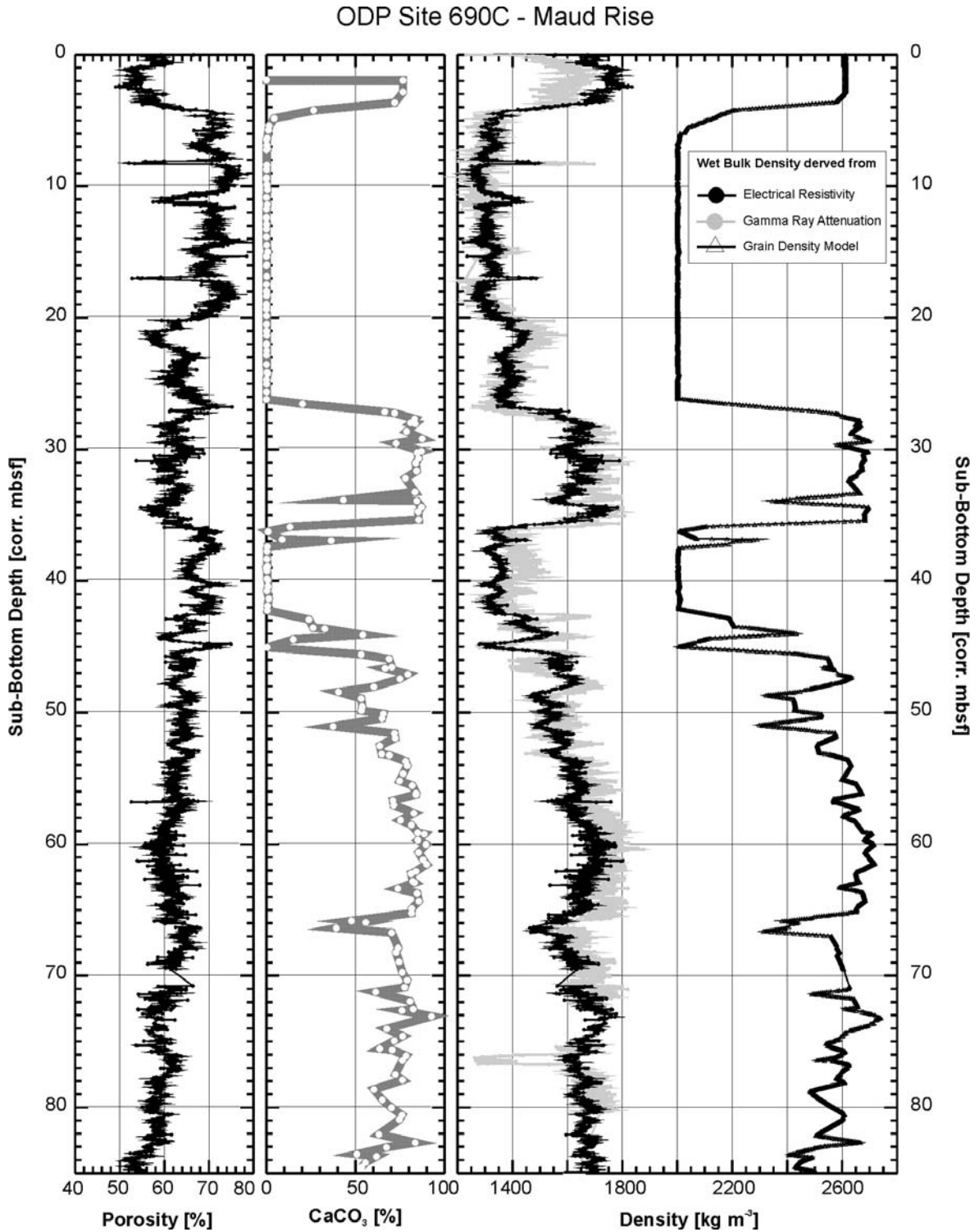
Fig. 2.9 Model based computation of a wet bulk density log from resistivity measurements on *ODP* core 690C. (a) Porosity log derived from formation factors having used Boyce's (1968) values for (a) and (m) in Archie's law. (b) Carbonate content (O'Conell 1990). (c) Wet bulk density log analyzed from gamma ray attenuation measurements onboard of JOIDES Resolution (gray curve). Superimposed is the wet bulk density log computed from electrical resistivity measurements on archive halves of the core (black curve) having used the grain density model shown in (d). Unpublished data from B. Laser and V. Spieß, University Bremen, Germany.

the centre of the coil (Gerland et al. 1993). This induced electric field contains information on the magnetic and electric properties of the sediment.

Generally, the coil characteristic is defined by the quality value(Q)

$$Q = \omega \cdot \frac{L(\omega)}{R(\omega)} \qquad (2.13)$$

(L(ω)) is the inductance, (R(ω)) the resistance and (ω) the (angular) frequency of the alternating current flowing through the coil (Chelkowski 1980). The inductance (L(ω)) depends on the number of windings, the length and diameter of the coil and the magnetic permeability of the coil material. The resistance (R(ω)) is a superposition of the resistance of the coil material and losses of the electric field induced in the core. It increases with decreasing resistivity in the sediment. Whether the inductance or the resistance is of major importance depends on the frequency of the current flowing through the coil. Changes in the inductance (L(ω)) can mainly be measured if currents of some kilohertz frequency or less are used. They simultaneously indicate variations in the magnetic susceptibility while the resistance (R(ω)) is insensitive to changes in the resistivity of the sediment. In contrast, operating with currents of several megahertz allows to measure the resistivity of the sediment by changes of the coil resistance (R(ω)) while variations in the

magnetic susceptibility do not affect the inductance (L(ω)). The examples presented here were measured with a commercial system (Scintrex CTU 2) which produces an output voltage that is proportional to the quality value (Q) of the coil at a frequency of 2.5 MHz, and after calibration is inversely proportional to the resistivity of the sediment.

The induced electric field is not confined to the coil position but extends over some sediment volume. Hence, measurements of the resistance (R(ω)) integrate over the resistivity distribution on both sides of the coil and provide a smoothed, low-pass filtered resistivity record. The amount of sediment volume affected by the induction process increases with larger coil diameters. The shape of the smoothing function can be measured from the impulse response of a thin metal plate glued in an empty plastic core liner. For a coil of about 14 cm diameter this gaussian-shaped function has a half-width of 4 cm (Fig. 2.10), so that the effect of an infinitely small resistivity anomaly is smeared over a depth range of 10 - 15 cm. This smoothing effect is equivalent to convolution of a source wavelet with a reflectivity function in seismic applications and can accordingly be removed by deconvolution algorithms. However, only few applications from longcore paleomagnetic studies are known up to now (Constable and Parker 1991; Weeks et al. 1993).
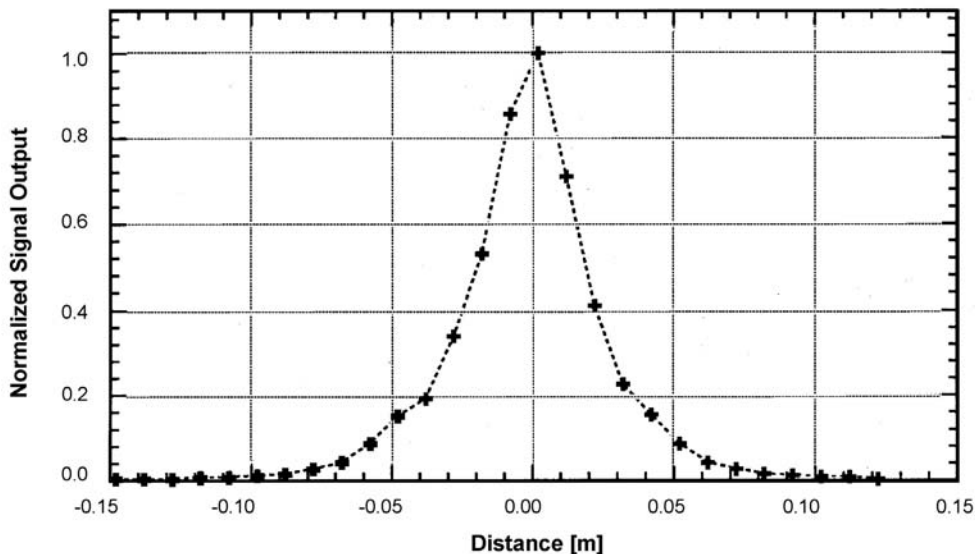

Fig. 2.10 Impulse response function of a thin metal plate measured by the inductive method with a coil of about 14 cm diameter. Modified after Gerland et al. (1993).

The low-pass filtering effect particularly becomes obvious if resistivity logs measured by the galvanic and inductive method are compared. Figure 2.11 displays such an example for a terrigenous core from the Weddell Sea (PS1635-1) and a biogenic foraminiferal and diatomaceous core from the Maud Rise (PS1836-3) in the Antarctic Ocean. Resistivities differ by maximum 15% (Fig. 2.11a), a rather high value which mainly results from core PS1635-1. Here, the downcore logs illustrate that the inductive methods produces lower resistivities than the galvanic method (Fig. 2.11b). In detail, the galvanic resistivity log reveals a lot of pronounced, fine-scale variations which cannot be resolved by induction measurements but are smeared along the core depth. For the biogenic core PS1836-3 this smoothing is not so important because lithology changes more gradually.

2.3   Permeability

Permeability describes how easy a fluid flows through a porous medium. Physically it is defined by Darcy's law

$$q = \frac{\kappa}{\eta} \cdot \frac{\partial p}{\partial x} \qquad (2.14)$$

which relates the flow rate (q) to the permeability (κ) of the pore space, the viscosity (η) of the pore fluid and the pressure gradient ($\partial p / \partial x$) causing the fluid flow. Simultaneously, permeability depends on the porosity (ϕ) and grain size distribution of the sediment, approximated by the mean grain size (d_m). Assuming that fluid flow can be simulated by an idealized flow through a bunch of capillaries with uniform radius ($d_m/2$) (Hagen Poiseuille's flow) permeabilities can for instance be estimated from Kozeny-Carman's equation (Carman 1956; Schopper 1982)

$$\kappa = \frac{d_m^2}{36k} \cdot \frac{\phi^3}{(1-\phi)^2} \qquad (2.15)$$

This relation is approximately valid for unconsolidated sediments of 30 - 80% porosity (Carman 1956). It is used for both geotechnical applications to estimate permeabilities of soil (Lambe and Whitman 1969) and seismic modeling of wave propagation in water-saturated sediments (Biot 1956a, b; Hovem and Ingram 1979; Hovem 1980;

Ogushwitz 1985). (κ) is a constant which depends on pore shape and tortuosity. In case of parallel, cylindrical capillaries it is about 2, for spherical sediment particles about 5, and in case of high porosities $\geq$ 10 (Carman 1956).

However, this is only one approach to estimate permeabilities from porosities and mean grain sizes. Other empirical relations exist, particularly for regions with hydrocarbon exploration (e.g. Gulf of Mexico, Bryant et al. 1975) or fluid venting (e.g. Middle Valley, Fisher et al. 1994) which compute depth-dependent permeabilities from porosity logs or take the grain size distribution and clay content into account.

Direct measurements of permeabilities in unconsolidated marine sediments are difficult, and only few examples are published. They confine to measurements on discrete samples with a specially developed tool (Lovell 1985), to indirect estimations by resistivity measurements (Lovell 1985), and to consolidation tests on ODP cores using a modified medical tool (Olsen et al. 1985). These measurements are necessary to correct for the elastic rebound (MacKillop et al. 1995) and to determine intrinsic permeabilities at the end of each consolidation step (Fisher et al. 1994). In Section 2.4.2 a numerical modeling and inversion scheme is described which estimates permeabilities from P-wave attenuation and dispersion curves (c.f. also section 3.6).

2.4   Acoustic and Elastic Properties

Acoustic and elastic properties are directly concerned with seismic wave propagation in marine sediments. They encompass P- and S-wave velocity and attenuation and elastic moduli of the sediment frame and wet sediment. The most important parameter which controls size and resolution of sedimentary structures by seismic studies is the frequency content of the source signal. If the dominant frequency and bandwidth are high, fine-scale structures associated with pore space and grain size distribution affect the elastic wave propagation. This is subject of ultrasonic transmission measurements on sediment cores (Sects. 2.4 and 2.5). At lower frequencies larger scale features like interfaces with different physical properties above and below and bedforms like mud waves, erosion zones and channel levee systems are the dominant structures imaged
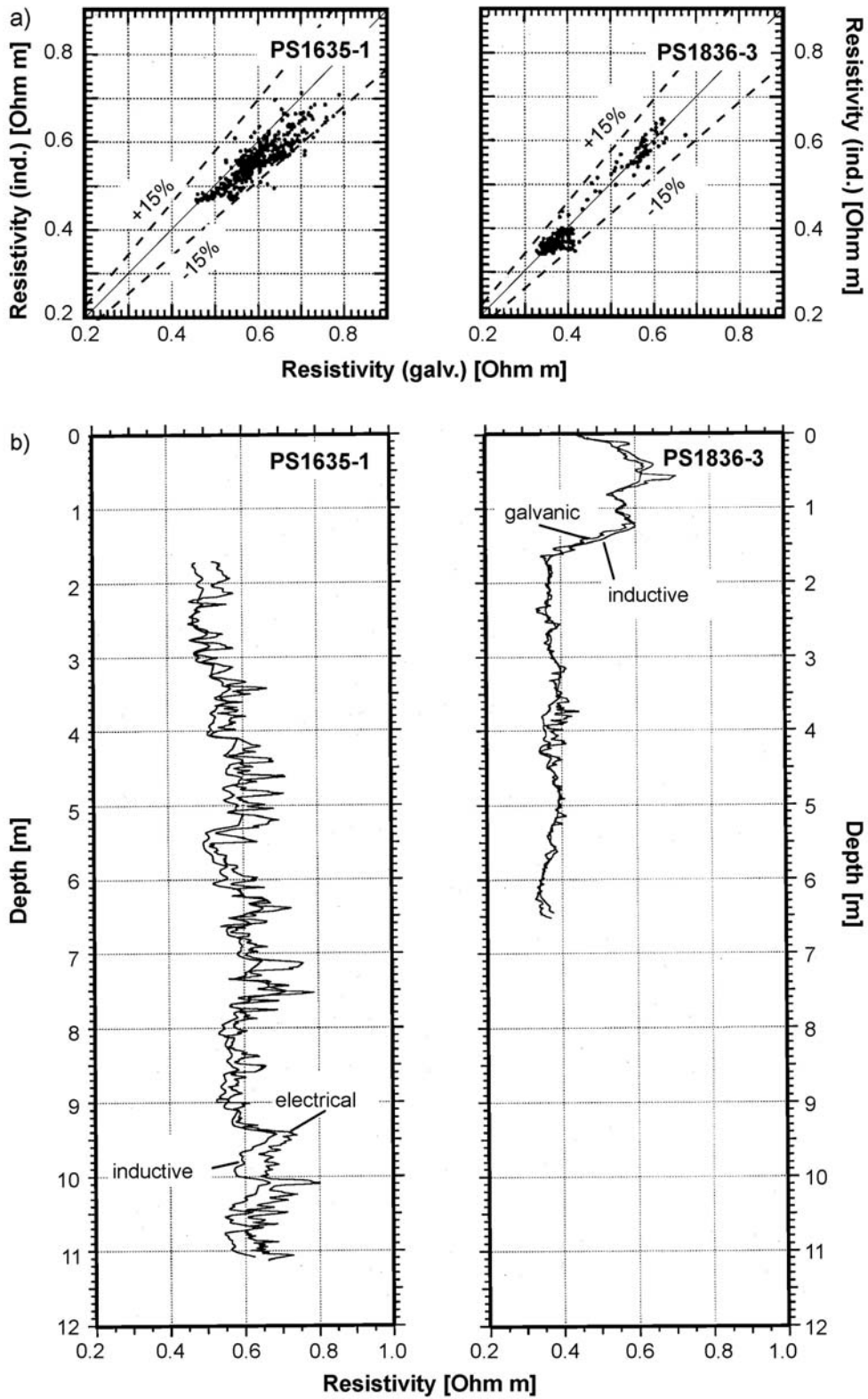
Fig. 2.11 Comparison of electrical resistivities (galv.) measured with the small hand-held probe and determined by the inductive method (ind.) for the gravity cores PS1635-1 and PS1836-3. (a) Cross plots of both data sets. The dashed lines indicate a difference of 15%. (b) Downcore resistivity logs determined by both methods. Modified after Gerland et al. (1993).

by sediment echosounder and multi-channel seismic surveys (Sect. 2.6).

In this section first Biot's viscoelastic model is summarized which simulates high- and low-frequency wave propagation in water-saturated sediments by computing phase velocity and attenuation curves. Subsequently, analysis techniques are introduced which derive P-wave velocities and attenuation coefficients from ultrasonic signals transmitted radially across sediment cores. Additional physical properties like S-wave velocity, elastic moduli and permeability are estimated by an inversion scheme.

2.4.1   Biot-Stoll Model

To describe wave propagation in marine sediments mathematically, various simple to complex models have been developed which approximate the sediment by a dilute suspension (Wood 1946) or an elastic, water-saturated frame (Gassmann 1951; Biot 1956a, b). The most common model which considers the microstructure of the sediment and simulates frequency-dependent wave propagation is based on Biot's theory (Biot 1956a, b). It includes Wood's suspension and Gassmann's elastic frame model as low-frequency approximations and combines acoustic and elastic parameters - P- and S-wave velocity and attenuation and elastic moduli - with physical and sedimentological parameters like mean grain size, porosity, density and permeability.

Based on Biot's fundamental work Stoll (e.g. 1974, 1977, 1989) reformulated the mathematical background of this theory with a simplified uniform nomenclature. Here, only the main physical principles and equations are summarized. For a detailed description please refer to one of Stoll's publications or Biot's original papers.

The theory starts with a description of the microstructure by 11 parameters. The sediment grains are characterized by their grain density (ρ_g) and bulk modulus (K_g), the pore fluid by its density (ρ_f), bulk modulus (K_f) and viscosity (η). The porosity (ϕ) quantifies the amount of pore space. Its shape and distribution are specified by the permeability (κ), a pore size parameter $a = d_m/3 \cdot \phi/(1-\phi)$, d_m = mean grain size (Hovem and Ingram 1979; Courtney and Mayer 1993), and structure factor $a' = 1 - r_0(1 - \phi^{-1})$ ($0 \leq r_0 \leq 1$) indicating a tortuosity of the pore space (Berryman 1980). The elasticity of the sediment frame is considered by its bulk and shear modulus (K_m and μ_m).

An elastic wave propagating in water-saturated sediments causes different displacements of the pore fluid and sediment frame due to their different elastic properties. As a result (global) fluid motion relative to the frame occurs and can approximately be described as Poiseuille's flow. The flow rate follows Darcy's law and depends on the permeability and viscosity of the pore fluid. Viscous losses due to an interstitial pore water flow are the dominant damping mechanism. Intergranular friction or local fluid flow can additionally be included but are of minor importance in the frequency range considered here.

Based on generalized Hooke's law and Newton's 2. Axiom two equations of motions are necessary to quantify the different displacements of the sediment frame and pore fluid. For P-waves they are (Stoll 1989)

$$\nabla^2 (H \cdot e - C \cdot \zeta) = \frac{\partial^2}{\partial t^2} (\rho \cdot e - \rho_f \cdot \zeta)$$

(2.16a)

$$\nabla^2 (C \cdot e - M \cdot \zeta) = \frac{\partial^2}{\partial t^2} (\rho_f \cdot e - m \cdot \zeta) - \frac{\eta}{\kappa} \cdot \frac{\partial \zeta}{\partial t}$$

(2.16b)

Similar equations for S-waves are given by Stoll (1989). Equation 2.16a describes the motion of the sediment frame and Equation 2.16b the motion of the pore fluid relative to the frame.

$$e = div(\vec{u})$$ (2.16c)

and

$$\zeta = \phi \cdot div(\vec{u} - \vec{U})$$ (2.16d)

are the dilatations of the frame and between pore fluid and frame ($\vec{u}$ = displacement of the frame, $\vec{U}$ = displacement of the pore fluid). The term ($\eta/\kappa \cdot \partial \zeta/\partial t$) specifies the viscous losses due to global pore fluid flow, and the ratio (η/κ) the viscous flow resistance.

The coefficients (H), (C), and (M) define the elastic properties of the water-saturated model. They are associated with the bulk and shear moduli of the sediment grains, pore fluid and sediment frame (K_g), (K_f), (K_m), (μ_m) and with the porosity (ϕ) by

$$H = (K_g - K_m)^2 / (D - K_m) + K_m + {}^4/_3 \cdot \mu_m$$ (2.17a)

$$C = (K_g \cdot (K_g - K_m)) / (D - K_m)$$ (2.17b)

$$M = K_g{}^2 / (D - K_m) \qquad (2.17c)$$

$$D = K_g \cdot (1 + \phi \cdot (K_g/K_f - 1)) \qquad (2.17d)$$

The apparent mass factor $m = a' \cdot \rho_f/\phi$ ($a' \geq 1$) in Equation 2.16b considers that not all of the pore fluid moves along the maximum pressure gradient in case of tortuous, curvilinear capillaries. As a result the pore fluid seems to be more dense, with higher inertia. (a') is called structure factor and is equal to 1 in case of uniform parallel capillaries.

In the low frequency limit H - $4/3\mu_m$ (Eq. 2.17a) represents the bulk modulus computed by Gassmann (1951) for a 'closed system' with no pore fluid flow. If the shear modulus (μ_m) of the frame is additionally zero, the sediment is approximated by a dilute suspension and Equation 2.17a reduces to the reciprocal bulk modulus of Wood's equation for 'zero' acoustic frequency, ($K^{-1} = \phi/K_f + (1-\phi)/K_g$; Wood 1946).

Additionally, Biot (1956a, b) introduced a complex correction function (F) which accounts for a frequency-dependent viscous flow resistance (η/κ). In fact, while the assumption of an ideal Poiseuille flow is valid for lower frequencies, deviations of this law occur at higher frequencies. For short wavelengths the influence of pore fluid viscosity confines to a thin skin depth close to the sediment frame, so that the pore fluid seems to be less viscous. To take these effects into account the complex function (F) modifies the viscous flow resistance (η/κ) as a function of pore size, pore fluid density, viscosity and frequency. A complete definition of (F) can be found in Stoll (1989).

The equations of motions 2.16 are solved by a plane wave approach which leads to a 2 x 2 determinant for P-waves

$$\det \begin{pmatrix} H \cdot k^2 - \rho\omega^2 & \rho_f\omega^2 - C \cdot k^2 \\ C \cdot k^2 - \rho_f\omega^2 & m\omega^2 - M \cdot k^2 - i\omega F\eta/\kappa \end{pmatrix} = 0$$

$$(2.18)$$

and a similar determinant for S-waves (Stoll 1989). The variable $k(\omega) = k_r(\omega) + ik_i(\omega)$ is the complex wavenumber. Computations of the complex zeroes of the determinant result in the phase velocity $c(\omega) = \omega/k_r(\omega)$ and attenuation coefficient $\alpha(\omega) = k_i(\omega)$ as real and imaginary parts. Generally, the determinant for P-waves has two and that for S-

waves one zero representing two P- and one S-wave propagating in the porous medium. The first P-wave (P-wave of first kind) and the S-wave are well known from conventional seismic wave propagation in homogeneous, isotropic media. The second P-wave (P-wave of second kind) is similar to a diffusion wave which is exponentially attenuated and can only be detected by specially arranged experiments (Plona 1980).

An example of such frequency-dependent phase velocity and attenuation curves presents Figure 2.12 for P- and S-waves together with the slope (power (n)) of the attenuation curves ($\alpha = k \cdot f^n$). Three sets of physical properties representing typical sand, silt and clay (Table 2.2) were used as model parameters. The attenuation coefficients show a significant change in their frequency dependence. They follow an $\alpha \sim f^2$ power law for low and an $\alpha \sim \sqrt{f}$ law for high frequencies and indicate a continuously decreasing power (n) (from 2 to 0.5) near a characteristic frequency $f_c = (\eta\phi)/(2\pi\kappa\rho_f)$. This characteristic frequency depends on the microstructure (porosity (ϕ), permeability (κ)) and pore fluid (viscosity (η), density (ρ_f)) of the sediment and is shifted to higher frequencies if porosity increases and permeability decreases. Below the characteristic frequency the sediment frame and pore fluid moves in phase and coupling between solid and fluid components is at maximum. This behaviour is typical for clayey sediments in which low permeability and viscous friction prevent any relative movement between pore fluid and frame up to several MHz, in spite of their high porosity. With increasing permeability and decreasing porosity the characteristic frequency diminishes so that in sandy sediments movements in phase only occur up to about 1 kHz. Above the characteristic frequency wavelengths are short enough to cause relative motions between pore fluid and frame.

Phase velocities are characterized by a low- and high-frequency plateau with constant values and a continuous velocity increase near the characteristic frequency. This dispersion is difficult to detect because it is confined to a small frequency band. Here, dispersion could only be detected from 1 - 10 kHz in sand, from 50 - 500 kHz in silt and above 100 MHz in clay. Generally, velocities in coarse-grained sands are higher than in fine-grained clays.

S-waves principally exhibit the same attenuation and velocity characteristics as P-waves. However, at the same frequency attenuation is
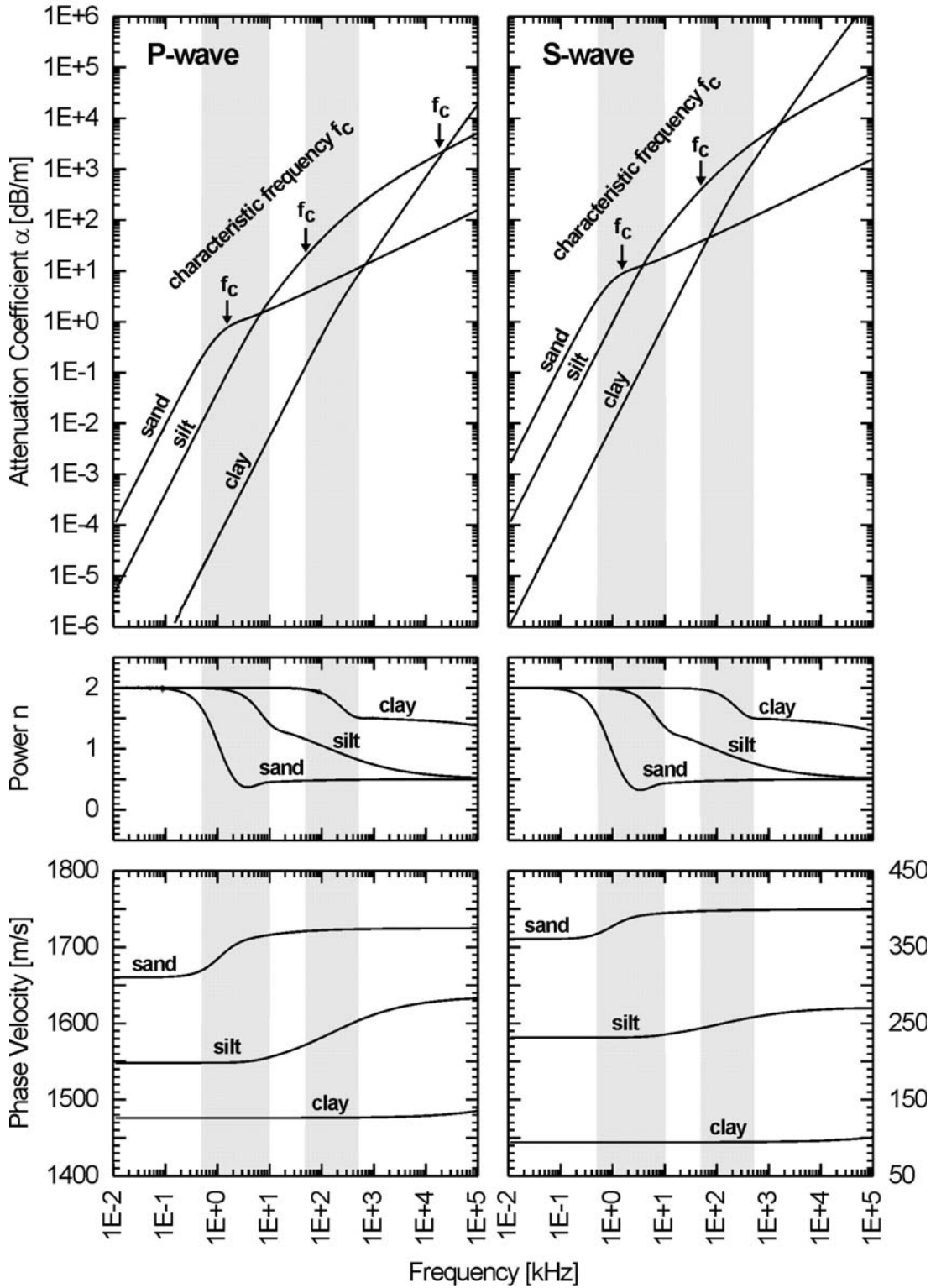
Fig. 2.12 Frequency-dependent attenuation and phase velocity curves and power (n) of the attenuation law $\alpha = k \cdot f^n$ computed for P-and S-waves in typical sand, silt and clay. The gray-shaded areas indicate frequency bands typical for ultrasonic measurements on sediment cores (50 - 500 kHz) and sediment echosounder surveys (0.5 - 10 kHz). Modified after Breitzke (1997).

about one magnitude higher, and velocities are significantly lower than for P-waves. The consequence is that S-waves are very difficult to record due to their high attenuation, though they are of great value for identifying fine-scale variations in the elasticity and microstructure of marine sediments. This is even valid if the low S-wave velocities are taken into account and lower frequencies are used for S-wave measurements than for P-wave recordings.

The two gray-shaded areas in Figure 2.12 mark two frequency bands typical for ultrasonic studies on sediment cores (50 - 500 kHz) and sediment echosounder surveys (0.5 - 10 kHz). They are displayed in order to point to one characteristic of acoustic measurements. Attenuation coefficients analyzed from ultrasonic measurements on sediment cores cannot directly be transferred to

sediment echosounder or seismic surveys. Primarily they only reflect the microstructure of the sediment. Rough estimates of the attenuation in seismic recordings from ultrasonic core measurements can be derived if ultrasonic attenuation is modeled, and attenuation coefficients are extrapolated to lower frequencies by such model curves.

2.4.2 Full Waveform Ultrasonic Core Logging

To measure the P-wave velocity and attenuation illustrated by Biot-Stoll's model an automated, PC-controlled logging system was developed which records and stores digital ultrasonic P-waveforms transmitted radially across marine sediment cores (Breitzke and Spieß 1993). These transmission measurements can be done at arbitrary small depth

Table 2.2 Physical properties of sediment grains, pore fluid and sediment frame used for the computation of attenuation and phase velocity curves according to Biot-Stoll's sediment model (Fig. 2.12).

Parameter	Sand	Silt	Clay
Sediment Grains			
Bulk Modulus K_g [10^9 Pa]	38	38	38
Density ρ_g [g cm^{-3}]	2.67	2.67	2.67
Pore Fluid			
Bulk Modulus K_f [10^9 Pa]	2.37	2.37	2.37
Density ρ_f [g cm^{-3}]	1.024	1.024	1.024
Viscosity η [10^{-3} Pa·s]	1.07	1.07	1.07
Sediment Frame			
Bulk Modulus K_m [10^6 Pa]	400	150	20
Shear Modulus μ_m [10^6 Pa]	240	90	12
Poisson Ratio σ_m	0.25	0.25	0.25
Pore Space			
Porosity ϕ [%]	50	60	80
Mean Grain Size d_m [10^{-6} m]	70	30	2
Permeability κ [m^2]	$5.4 \cdot 10^{-11}$	$2.3 \cdot 10^{-12}$	$7.1 \cdot 10^{-15}$
Pore Size Parameter $a = d_m / 3 \phi /(1-\phi)$ [10^{-6} m]	23	15	2.7
Ratio κ / a^2	0.1	0.01	0.001
Structure Factor $a' = 1 - r_0 (1 - \phi^{-1})$	1.5	1.3	1.1
Constant r_0	0.5	0.5	0.5

Fig. 2.13 Full waveform ultrasonic core logging, from lithology controlled single traces to the gray shaded pixel graphic of transmission seismograms, and P-wave velocity and attenuation logs derived from the transmission data. The single traces on the left-hand side reflect true amplitudes while the wiggle traces of the core segment and the pixel graphic are normalized to maximum values. Data from Breitzke et al. (1996).

increments so that the resulting seismogram sections can be combined to an ultrasonic image of the core.

Figure 2.13 displays the most prominent effects involved in full waveform ultrasonic core logging. Gravity core GeoB1510-2 from the western equatorial South Atlantic serves as an example. The lithology controlled single traces and amplitude spectra demonstrate the influence of increasing grain sizes on attenuation and frequency content of transmission seismograms. Compared to a reference signal in distilled water, the signal shape remains almost unchanged in case of wave propagation in fine-grained clayey sediments (1st attenuated trace). With an increasing amount of silty and sandy particles the signal amplitudes are reduced due to an enhanced attenuation of high-frequency components (2nd and 3rd attenuated trace). This attenuation is accompanied by a change in signal shape, an effect which is particularly obvious in the normalized wiggle trace display of the 1 m long core segment. While the upper part of this segment is composed of fine-grained nannofossil ooze, a calcareous foraminiferal turbidite occurs in the lower part. The downward coarsening of the graded bedding causes successively lower-frequency signals which can easily be distinguished from the high-frequency transmission seismograms in the upper fine-grained part. Additionally, first arrival times are lower in the coarse-grained turbidite than in fine-grained nannofossil oozes indicating higher velocities in silty and sandy sediments than in the clayey part. A conversion of the normalized wiggle traces to a gray-shaded pixel graphic allows us to present the full transmission seismogram information on a handy scale. In this ultrasonic image of the sediment core lithological changes appear as smooth or sharp phase discontinuities resulting from the low-frequency waveforms in silty and sandy layers. Some of these layers indicate a graded bedding by downward prograding phases (1.60 - 2.10 m, 4.70 - 4.80 m, 7.50 - 7.60 m). The P-wave velocity and attenuation log analyzed from the transmission seismograms support the interpretation. Coarse-grained sandy layers are characterized by high P-wave velocities and attenuation coefficients while fine-grained parts reveal low values in both parameters. Especially, attenuation coefficients reflect lithological changes much more sensitively than P-wave velocities.

While P-wave velocities are determined online during core logging using a cross-correlation technique for the first arrival detection (Breitzke and Spieß 1993)

$$v_P = \frac{d_{outside} - 2d_{liner}}{t - 2t_{liner}} \qquad (2.19)$$

($d_{outside}$ = outer core diameter, 2 d_{liner} = double liner wall thickness, t = detected first arrival, $2t_{liner}$ = travel time across both liner walls), attenuation coefficients are analyzed by a post-processing routine. Several notches in the amplitude spectra of the transmission seismograms caused by the resonance characteristics of the ultrasonic transducers required a modification of standard attenuation analysis techniques (e.g. Jannsen et al. 1985; Tonn 1989, 1991). Here, a modification of the spectral ratio method is applied (Breitzke et al. 1996). It defines a window of bandwidth ($b_i = f_{ui} - f_{li}$) in which the spectral amplitudes are summed (Fig. 2.14a).

$$\overline{A}(f_{mi}, x) = \sum_{f_i = f_{li}}^{f_{ui}} A(f_i, x) \qquad (2.20)$$

The resulting value ($\overline{A}(f_{mi}, x)$) is related to that part of the frequency band which predominantly contributes to the spectral sum, i.e. to the arithmetic mean frequency (f_{mi}) of the spectral amplitude distribution within the ith band. Subsequently, for a continuously moving window a series of attenuation coefficients ($\alpha(f_{mi})$) is computed from the natural logarithm of the spectral ratio of the attenuated and reference signal

$$\alpha(f_{mi}) = \ln\left[\frac{\overline{A}(f_{mi}, x)}{\overline{A}_{ref}(f_{mi}, x)}\right] \Big/ x = k \cdot f^n \qquad (2.21)$$

Plotted in a log α - log f diagram the power (n) and logarithmic attenuation factor (log k) can be determined from the slope and intercept of a linear least square fit to the series of ($f_{mi}, \alpha(f_{mi})$) pairs (Fig. 2.14b). Finally, a smoothed attenuation coefficient $\alpha(f) = k \cdot f^n$ is calculated for the frequency (f) using these values for (k) and (n).

Figure 2.14b shows several attenuation curves ($\alpha(f_{mi})$) analyzed along the turbidite layer of core GeoB1510-2. With downward-coarsening grain sizes attenuation coefficients increase. Each linear regression to one of these curves provide a power (n) and attenuation factor (k), and thus one value $\alpha = k \cdot f^n$ on the attenuation log of the complete core (Fig. 2.14c).
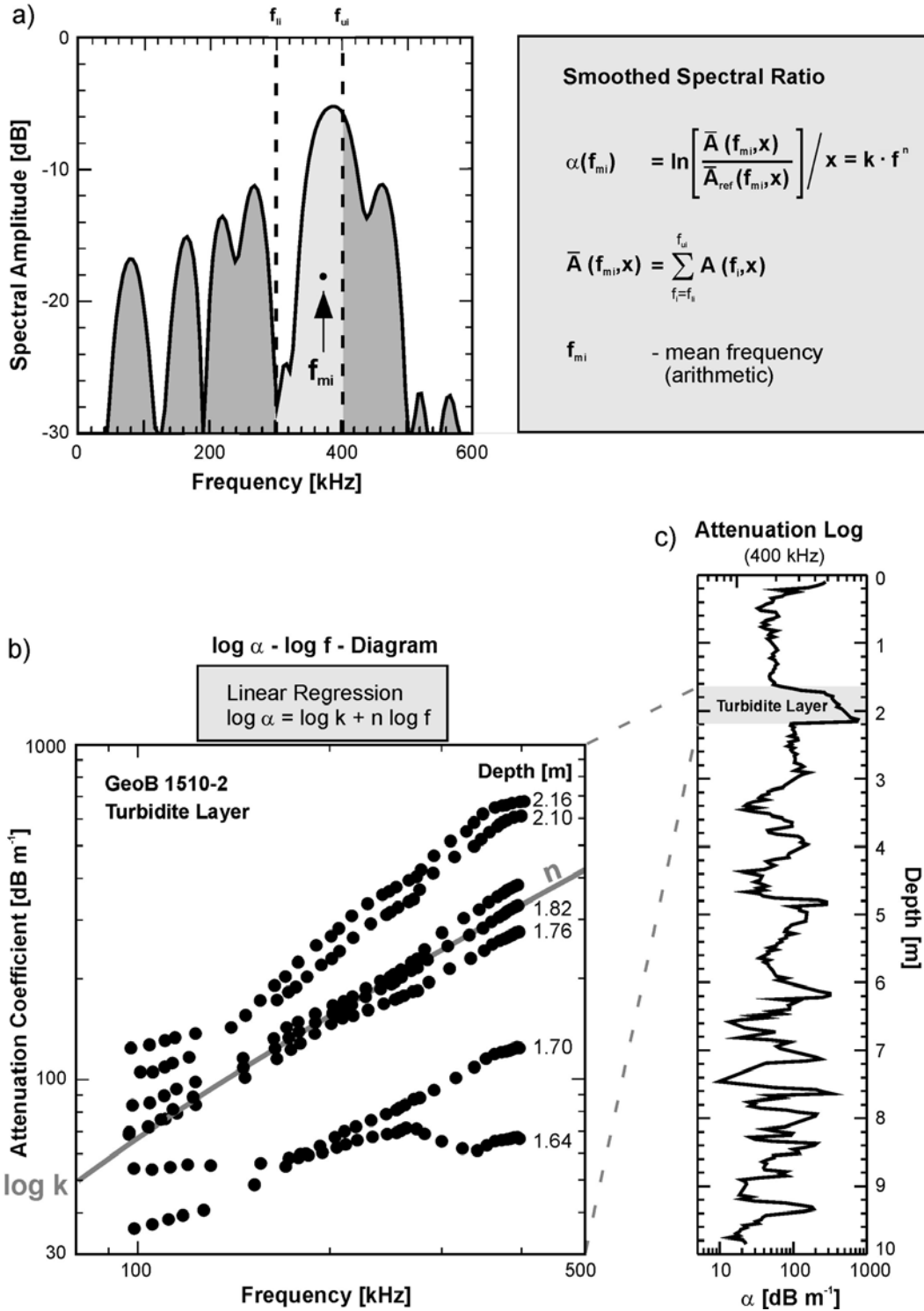
ATTENUATION ANALYSIS

a)

Smoothed Spectral Ratio

$$\alpha(f_{mi}) = \ln\left[\frac{\bar{A}(f_{mi},x)}{\bar{A}_{ref}(f_{mi},x)}\right]\bigg/ x = k \cdot f^n$$

$$\bar{A}(f_{mi},x) = \sum_{f_i=f_{li}}^{f_{ui}} A(f_i,x)$$

f_{mi} - mean frequency (arithmetic)

b)

log α - log f - Diagram

Linear Regression
log α = log k + n log f

GeoB 1510-2
Turbidite Layer

Depth [m]
2.16
2.10
1.82
1.76
1.70
1.64

c) **Attenuation Log**
(400 kHz)

Fig. 2.14 Attenuation analysis by the smoothed spectral ratio method. (a) Definition of a moving window of bandwidth $b_i = f_{ui} - f_{li}$, in which the spectral amplitudes are summed. (b) Seven attenuation curves analyzed from the turbidite layer of gravity core GeoB1510-2 and linear regression to the attenuation curve in 1.82 m depth. (c) Attenuation log of gravity core GeoB1510-2 for 400 kHz frequency. Data from Breitzke et al. (1996).

As the P-wave attenuation coefficient obviously depends on the grain size distribution of the sediment it can be used as a proxy parameter for the mean grain size, i.e. for a sedimentological parameter which is usually only measured at coarse increments due to the time-consuming grain size analysis methods. For instance, this can be of major importance in current controlled sedimentation environments where high-resolution grain size logs might indicate reduced or enhanced current intensities.

If the attenuation coefficients and mean grain sizes analyzed on discrete samples of core GeoB1510-2 are displayed as a cross plot a second order polynomial can be derived from a least square fit (Fig. 2.15a). This regression curve then allows to predict mean grain sizes using the attenuation coefficient as proxy parameter. The accuracy of the predicted mean grain sizes illus-

trates the core log in Figure 2.15b. The predicted gray shaded log agrees well with the superimposed dots of the measured data.

Similarly, P-wave velocities can also be used as proxy parameters for a mean grain size prediction. However, as they cover only a small range (1450 - 1650 m/s) compared to attenuation coefficients (20 - 800 dB/m) they reflect grain size variations less sensitively.

Generally, it should be kept in mind, that the regression curve in Figure 2.15 is only an example. Its applicability is restricted to that range of attenuation coefficients for which the regression curve was determined and to similar sedimentation environments (calcareous foraminiferal and nannofossil ooze). For other sediment compositions new regression curves must be determined, which are again only valid for that specific sedimentological setting.
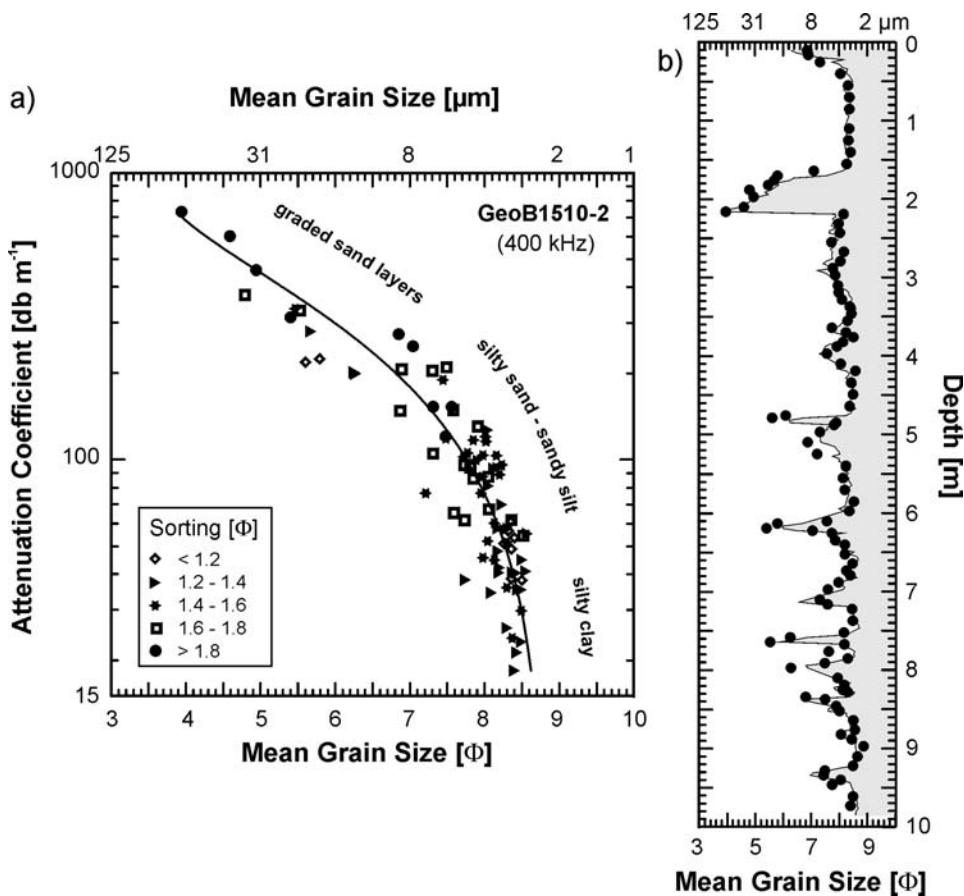

Fig. 2.15 (a) Attenuation coefficients (at 400 kHz) of gravity core GeoB1510-2 versus mean grain sizes. The solid line indicates a second degree polynomial used to predict mean grain sizes from attenuation coefficients. (b) Comparison of the predicted mean grain size log (gray shaded) with the data measured on discrete samples (solid dots). Mean grain sizes are given in $\Phi = -log_2 d$, d = grain diameter in mm. Modified after Breitzke et al. (1996).

Biot-Stoll's theory allows us to model P-wave velocities and attenuation coefficients analyzed from transmission seismograms. As an example Figure 2.16 displays six data sets for the turbidite layer of core GeoB1510-2. While attenuation coefficients were analyzed as described above frequency dependent P-wave velocities were determined from successive bandpass filtered transmission seismograms (Courtney and Mayer 1993; Breitzke 1997). Porosities and mean grain sizes enter the modeling computations via the pore size parameter (a) and structure factor (a'). Physical properties of the pore fluid and sediment grains are the same as given in Table 2.2. A bulk and shear modulus of 10 and 6 MPa account for the elasticity of the frame. As the permeability is the parameter which is usually unknown but has the strongest influence on attenuation and velocity dispersion, model curves were computed for three constant ratios $\kappa/a^2 = 0.030$, 0.010 and 0.003 of permeability (κ) and pore size parameter (a). The resulting permeabilities are given in each diagram. These theoretical curves show that the attenuation and velocity data between 170 and 182 cm depth can consistently be modeled by an appropriate set of input parameters. Viscous losses due to a global pore water flow through the sediment are sufficient to explain the attenuation in these sediments. Only if the turbidite base is approached (188 - 210 cm depth) the attenuation and velocity dispersion data successively deviate from the model curves probably due to an increasing amount of coarse-grained foraminifera. An additional damping mechanism which

might either be scattering or resonance within the hollow foraminifera must be considered.

Based on this modeling computations an inversion scheme was developed which automatically iterates the permeability and minimizes the difference between measured and modeled attenuation and velocity data in a least square sense (Courtney and Mayer 1993; Breitzke 1997). As a result S-wave velocities and attenuation coefficients, permeabilities and elastic moduli of water-saturated sediments can be estimated. They are strictly only valid if attenuation and velocity dispersion can be explained by viscous losses. In coarse-grained parts deviations must be taken into account for the estimated parameters, too. Applied to the data of core GeoB1510-2 in 170, 176 and 182 cm depth S-wave velocities of 67, 68 and 74 m/s and permeabilities of $5 \cdot 10^{-13}$, $1 \cdot 10^{-12}$ and $3 \cdot 10^{-12}$ m^2 result from this inversion scheme.

2.5   Sediment Classification

Full waveform ultrasonic core logging was applied to terrigenous and biogenic sediment cores to analyze P-wave velocities and attenuation coefficients typical for the different settings. Together with the bulk parameters and the physical properties estimated by the inversion scheme they form the data base for a sediment classification which identifies different sediment types from their

Table 2.3 Geographical coordinates, water depth, core length, region and composition of the sediment cores considered for the sediment classification in Section 2.5.

Core	Coordinates	Water Depth	Core Length	Region	Sediment Composition
40KL	07°33.1'N 85°29.7'E	3814 m	8.46 m	Bengal Fan	terrigenous clay, silt, sand
47KL	11°10.9'N 88°24.9'E	3293 m	10.00 m	Bengal Fan	terrigenous clay, silt, sand; foram. and nannofossil ooze
GeoB 2821-1	30°27.1'S 38°48.9'W	3941 m	8.19 m	Rio Grande Rise	foram. and nannofossil ooze
PS 2567-2	46°56.1'S 06°15.4'E	4102 m	17.65 m	Meteor Rise	diatomaceous mud/ooze; few foram. and nannofossil layers
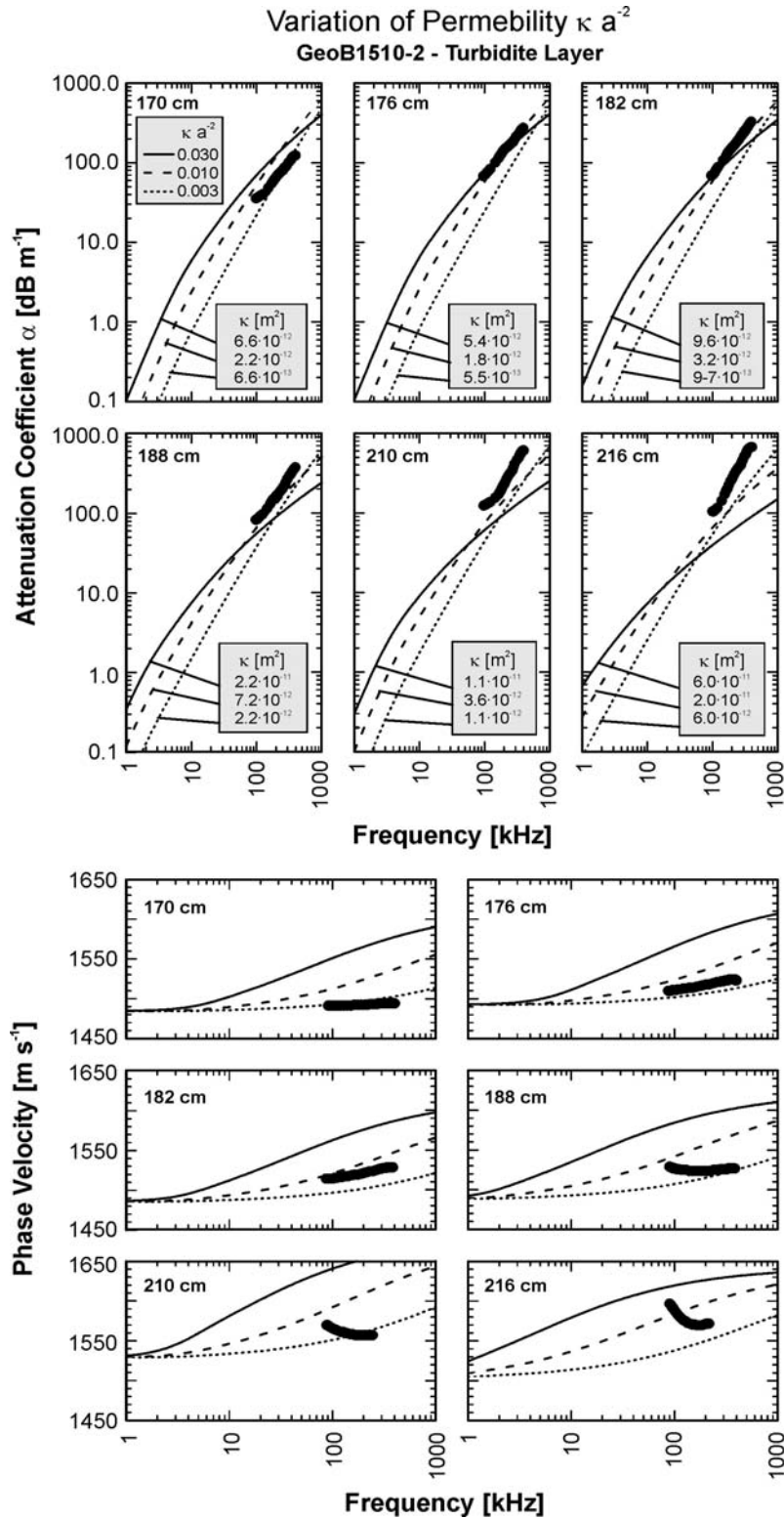
Fig. 2.16 Comparison of P-wave attenuation and velocity dispersion data derived from ultrasonic transmission seismograms with theoretical curves based on Biot-Stoll's model for six traces of the turbidite layer of gravity core GeoB1510-2. Permeabilities vary in the model curves according to constant ratios κ/a^2 = 0.030, 0.010, 0.003 (κ = permeability, a = pore size parameter). The resulting permeabilities are given in each diagram. Modified after Breitzke et al. (1996).

acoustic and elastic properties. Table 2.3 summarizes the cores used for this sediment classification.

2.5.1   Full Waveform Core Logs as Acoustic Images

That terrigenous, calcareous and biogenic siliceous sediments differ distinctly in their acoustic properties is shown by four transmission seismogram sections in Figure 2.17. Terrigenous sediments from the Bengal Fan (40KL, 47KL) are composed of upward-fining sequences of turbidites characterized by upward decreasing attenuations and P-wave velocities. Coarse-grained basal sandy layers can easily be located by low-frequency waveforms and high P-wave velocities.

Calcareous sediments from the Rio Grande Rise (GeoB2821-1) in the western South Atlantic also exhibit high- and low-frequency signals which scarcely differ in their P-wave velocities. In these sediments high-frequency signals indicate fine-grained nannofossil ooze while low-frequency signals image coarse-grained foraminiferal ooze.

The sediment core from the Meteor Rise (PS2567-2) in the Antarctic Ocean is composed of diatomaceous and foraminiferal-nannofossil ooze deposited during an advance and retreat of the Polar Frontal Zone in glacial and interglacial stages. Opal-rich, diatomaceous ooze can be identified from high-frequency signals while foraminiferal-nannofossil ooze causes higher attenuation and low-frequency signals. P-wave velocities again only show smooth variations.

Acoustic images of the complete core lithologies present the colour-encoded graphics of the transmission seismograms, in comparison to the lithology derived from visual core inspection (Fig. 2.18). Instead of normalized transmission seismograms instantaneous frequencies are displayed here (Taner et al. 1979). They reflect the dominant frequency of each transmission seismogram as time-dependent amplitude, and thus directly indicate the attenuation. Highly attenuated low-frequency seismograms appear as warm red to white colours while parts with low attenuation and high-frequency seismograms are represented by cool green to black colours.

In these attenuation images the sandy turbidite bases in the terrigenous cores from the Bengal Fan (40KL, 47KL) can easily be distinguished. Graded beddings can also be identified from slightly prograding phases and continuously decreasing travel times. In contrast, the transition to calcareous, pelagic sediments in the upper part (> 5.6 m) of core 47KL is rather difficult to detect. Only above 3.2 m depth a slightly increased attenuation can be observed by slightly warmer colours at higher transmission times (> 140 μs). In this part of the core (> 3.2 m) sediments are mainly composed of coarse-grained foraminiferal ooze, while farther downcore (3.2 - 5.6 m) fine-grained nannofossils prevail in the pelagic sediments.

The acoustic image of the calcareous core from the Rio Grande Rise (GeoB2821-1) shows much more lithological changes than the visual core description. Cool colours between 1.5 - 2.5 m depth indicate unusually fine grain sizes (Breitzke 1997). Alternately yellow/red and blue/black colours in the lower part of the core (> 6.0 m) reflect an interlayering of fine-grained nannofossil and coarse-grained foraminiferal ooze. Dating by orbital tuning shows that this interlayering coincides with the 41 ky cycle of obliquity (von Dobeneck and Schmieder 1999) so that fine-grained oozes dominate during glacial and coarse-grained oozes during interglacial stages.

The opal-rich diatomaceous sediments in core PS2567-2 from the Meteor Rise are characterized by a very low attenuation. Only 2 - 3 calcareous layers with significantly higher attenuation (yellow and red colours) can be identified as prominent lithological changes.

2.5.2   P- and S-Wave Velocity, Attenuation, Elastic Moduli and Permeability

As the acoustic properties of water-saturated sediments are strongly controlled by the amount and distribution of pore space, cross plots of P-wave velocity and attenuation coefficient versus porosity clearly indicate the different bulk and elastic properties of terrigenous and biogenic sediments and can thus be used for an acoustic classification of the lithology. Additional S-wave velocities (and attenuation coefficients) and elastic moduli estimated by least-square inversion specify the amount of bulk and shear moduli which contribute to the P-wave velocity (Breitzke 2000).

The cross plots of the P-wave parameters of the four cores considered above illustrate that terrigenous, calcareous and diatomaceous sediments can uniquely be identified from their position in both diagrams (Fig. 2.19). In terri-
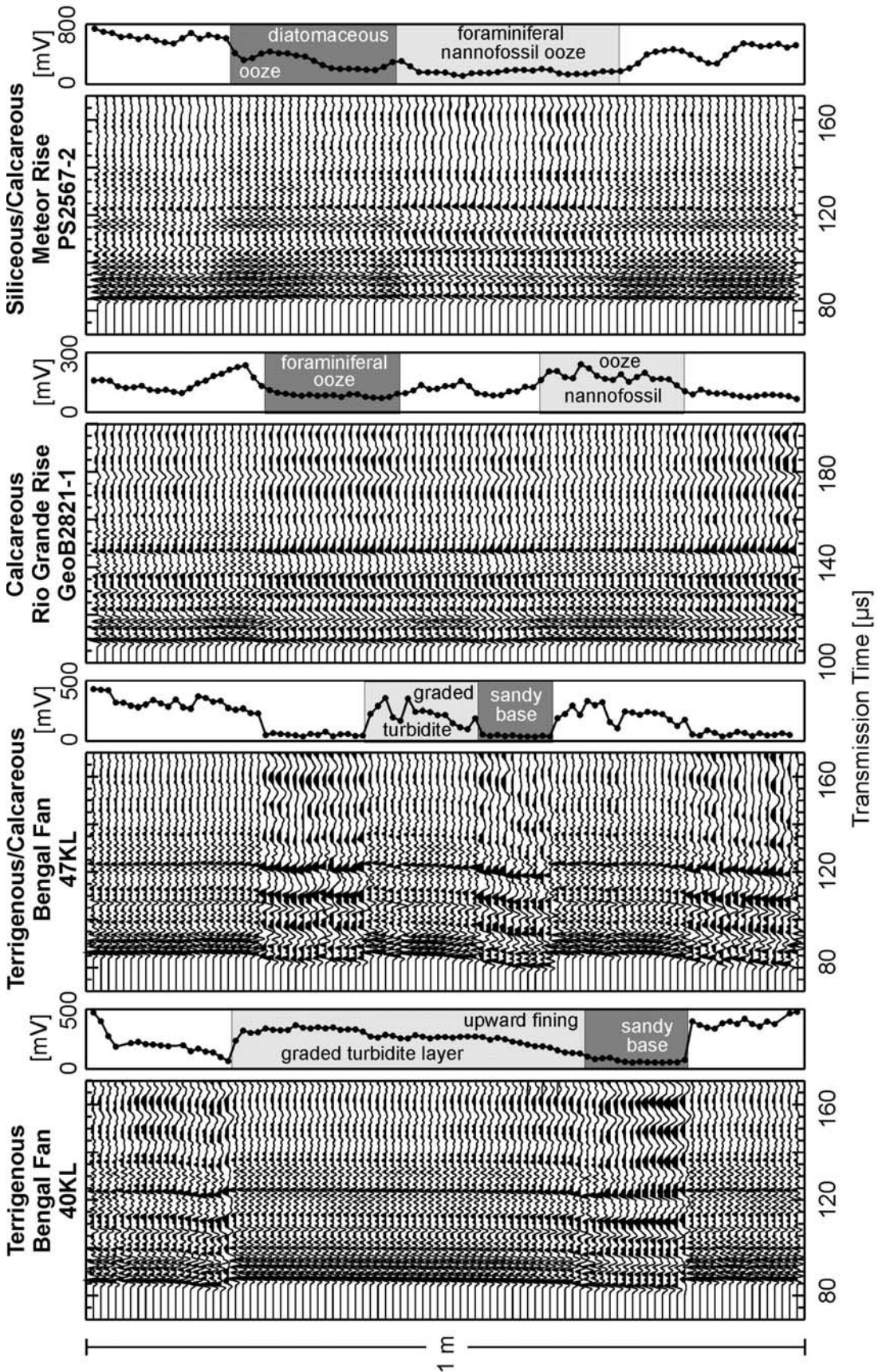
Fig. 2.17 Normalized transmission seismogram sections of four 1 m long core segments from different terrigenous and biogenic sedimentation environments. Seismograms were recorded with 1 cm spacing. Core depths are 5.49-6.43 m (40KL), 6.03-6.97 m (47KL), 5.26-6.14 m (GeoB2821-1), 12.77-13.60 m (PS2567-2). Maximum amplitudes of the transmission seismograms are plotted next to each section from 0 to ... mV, as given at the top.
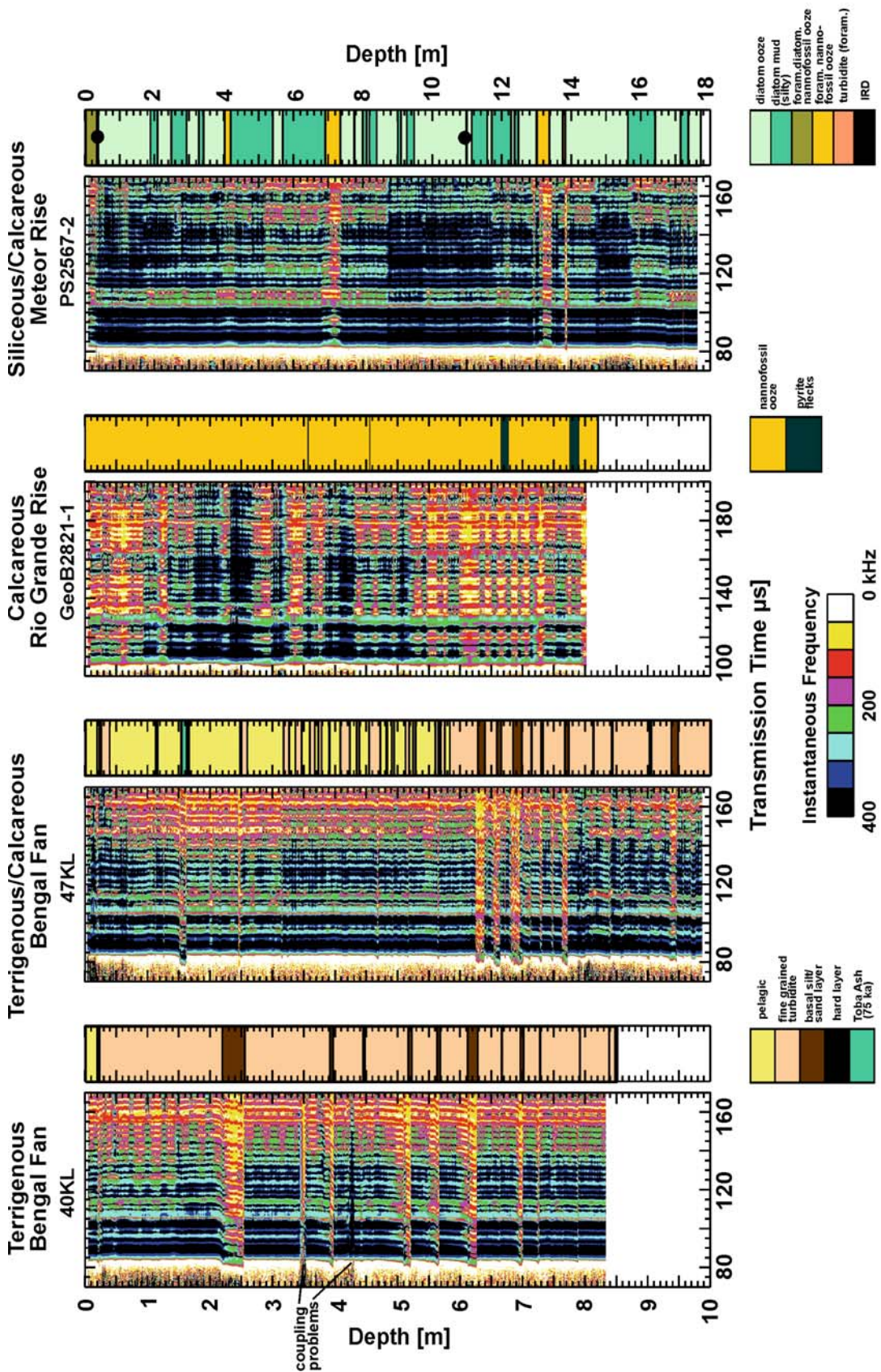
Fig. 2.18 Ultrasonic images of the transmission measurements on cores 40KL, 47KL, GeoB2821-1 and PS2567-2 retrieved from different terrigenous and biogenic sedimentation environments. Displayed are the colour-encoded instantaneous frequencies of the transmission seismograms and the lithology derived from visual core inspections.

genous sediments (40KL, 47KL) P-wave velocities and attenuation coefficients increase with decreasing porosities. Computed S-wave velocities are very low ($\approx$ 60 - 65 m s^{-1}) and almost independent of porosity (Fig. 2.20a) whereas computed S-wave attenuation coefficients (at 400 kHz) vary strongly from $4 \cdot 10^3$ dB m^{-1} in fine-grained sediments to $1.5 \cdot 10^4$ dB m^{-1} in coarse-grained sediments (Fig. 2.20b). Accordingly, shear moduli are also low and do not vary very much (Fig. 2.21b) so that higher P-wave velocities in terrigenous sediments mainly result from higher bulk moduli (Fig. 2.21a).

If calcareous, particularly foraminiferal components (FNO) are added to terrigenous sediments porosities become higher ($\approx$ 70 - 80%, 47KL). P-wave velocities slightly increase from their minimum of 1475 m s^{-1} at 70% porosity to 1490 m s^{-1} at 80% porosity (Fig. 2.19a) mainly due to an increase in the shear moduli from about 6.5 to 8.5 MPa whereas bulk moduli remain almost constant at about 3000 MPa (Fig. 2.21b). However, a much more pronounced increase can be observed in the P-wave attenuation coefficients (Fig. 2.19b). For porosities of about 80% they reach the same values (about 200 dB m^{-1}) as terrigenous sediments of about 55% porosity, but can easily be distinguished because of higher P-wave velocities in terrigenous sediments. S-wave attenuation coefficients increase as well in these hemipelagic sediments from about $1 \cdot 10^5$ dB m^{-1} at 65% porosity to about $2.5 \cdot 10^5$ dB m^{-1} at 80% porosity (Fig. 2.20b), and are thus even higher than in terrigenous sediments.

Calcareous foraminiferal and nannofossil oozes (NFO) show similar trends in both P-wave and S-wave parameters as terrigenous sediments, but are shifted to higher porosities due to their additional intraporosities (GeoB2821-1; Figs. 2.19, 2.20).

In diatomaceous oozes P- and S-wave wave velocities increase again though porosities are very high (>80%, PS2567-2; Figs. 2.19, 2.20). Here, the diatom shells build a very stiff frame which causes high shear moduli and S-wave velocities (Fig. 2.21). It is this increase in the shear moduli which only accounts for the higher P-wave velocities while the bulk moduli remain almost constant and are close to the bulk modulus of sea water (Fig. 2.21). P-wave attenuation coefficients are very low in these high-porosity sediments (Fig. 2.19b) whereas S-wave attenuation coefficients are highest (Fig. 2.20b).

Permeabilities estimated from the least square inversion mainly reflect the attenuation charac-

teristics of the different sediment types (Fig. 2.22). They reach lowest values of about $5 \cdot 10^{-14}$ m^2 in fine-grained clayey mud and nannofossil ooze. Highest values of about $5 \cdot 10^{-11}$ m^2 occur in diatomaceous ooze due to their high porosities. Nevertheless, it should be kept in mind that these permeabilities are only estimates based on the input parameters and assumptions incorporated in Biot-Stoll's model. For instance one of these assumptions is that only mean grain sizes are used, but the influence of grain size distributions is neglected. Additionally, the total porosity is usually used as input parameter for the inversion scheme without differentiation between inter- and intraporosities. Comparisons of these estimated permeabilities with direct measurements unfortunately do not exist up to know.

2.6 Sediment Echosounding

While ultrasonic measurements are used to study the structure and composition of sediment cores, sediment echosounders are hull-mounted acoustic systems which image the upper 10-200 m of sediment coverage by remote sensing surveys. They operate with frequencies around 3.5-4.0 kHz. The examples presented here were digitally recorded with the narrow-beam Parasound echosounder and ParaDIGMA recording system (Spieß 1993).

2.6.1 Synthetic Seismograms

Figure 2.23 displays a Parasound seismogram section recorded across an inactive channel of the Bengal Fan. The sediments of the terrace were sampled by a 10 m long piston core (47KL). Its acoustic and bulk properties can either be directly compared to the echosounder recordings or by computations of synthetic seismograms. Such modeling requires P-wave velocity and wet bulk density logs as input parameters. From the product of both parameters acoustic impedances $I = v_P \cdot \rho$ are calculated. Changes in the acoustic impedance cause reflections of the normally incident acoustic waves. The amplitude of such reflections is determined by the normal incidence reflection coefficient $R = (I_2 - I_1) / (I_2 + I_1)$, with ($I_1$) and ($I_2$) being the impedances above and below the interface. From the series of reflection coefficients the reflectivity can be computed as impulse response function, including all internal
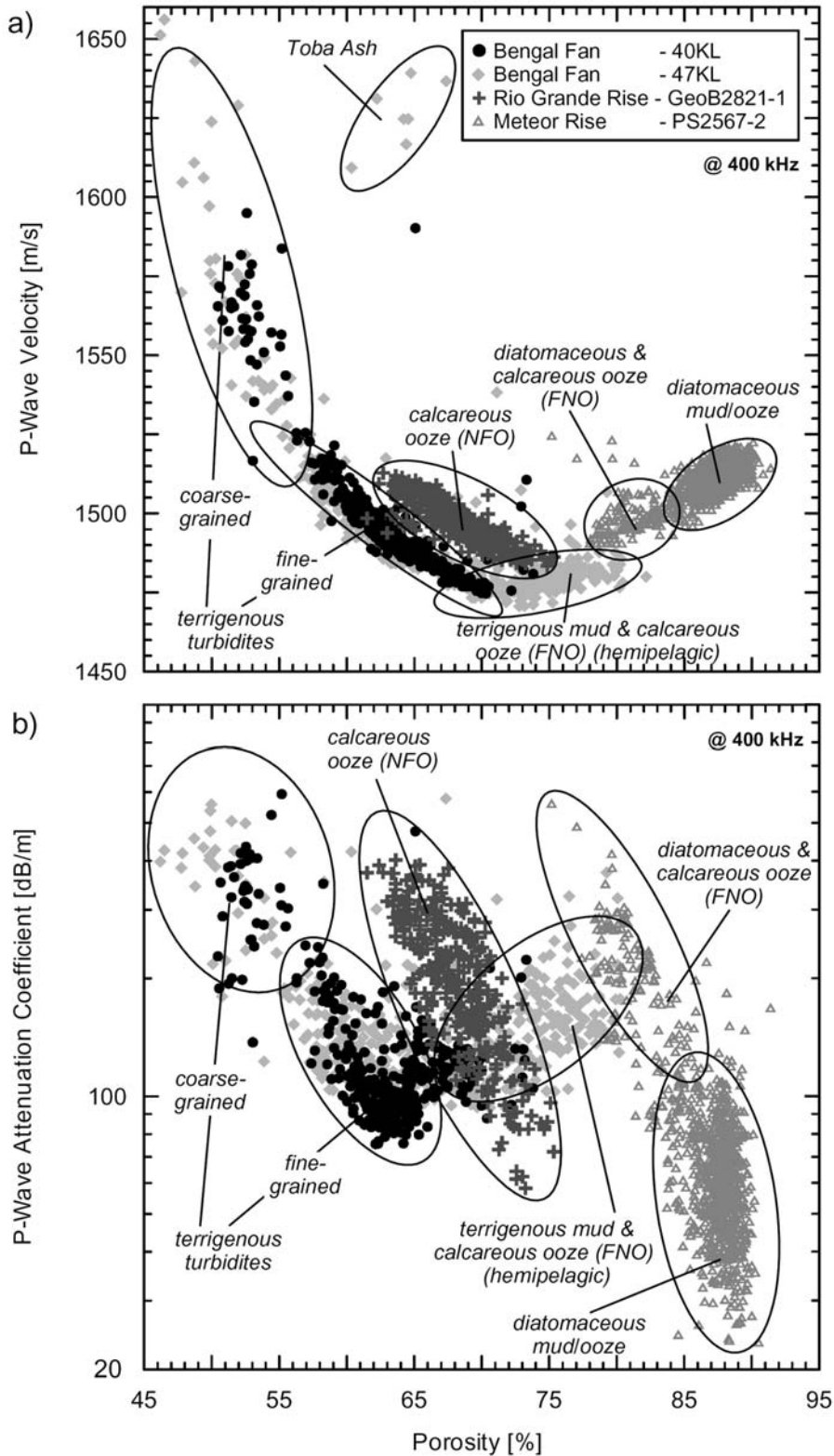
Fig. 2.19 (a) P-wave velocities and (b) attenuation coefficients (at 400 kHz) versus porosities for the four sediment cores 40KL, 47KL, GeoB2821-1, and PS2567-2. NFO is nannofossil foraminiferal ooze, FNO is foraminiferal nannofossil ooze (nomenclature after Mazullo et al. (1988)). Modified after Breitzke (2000).
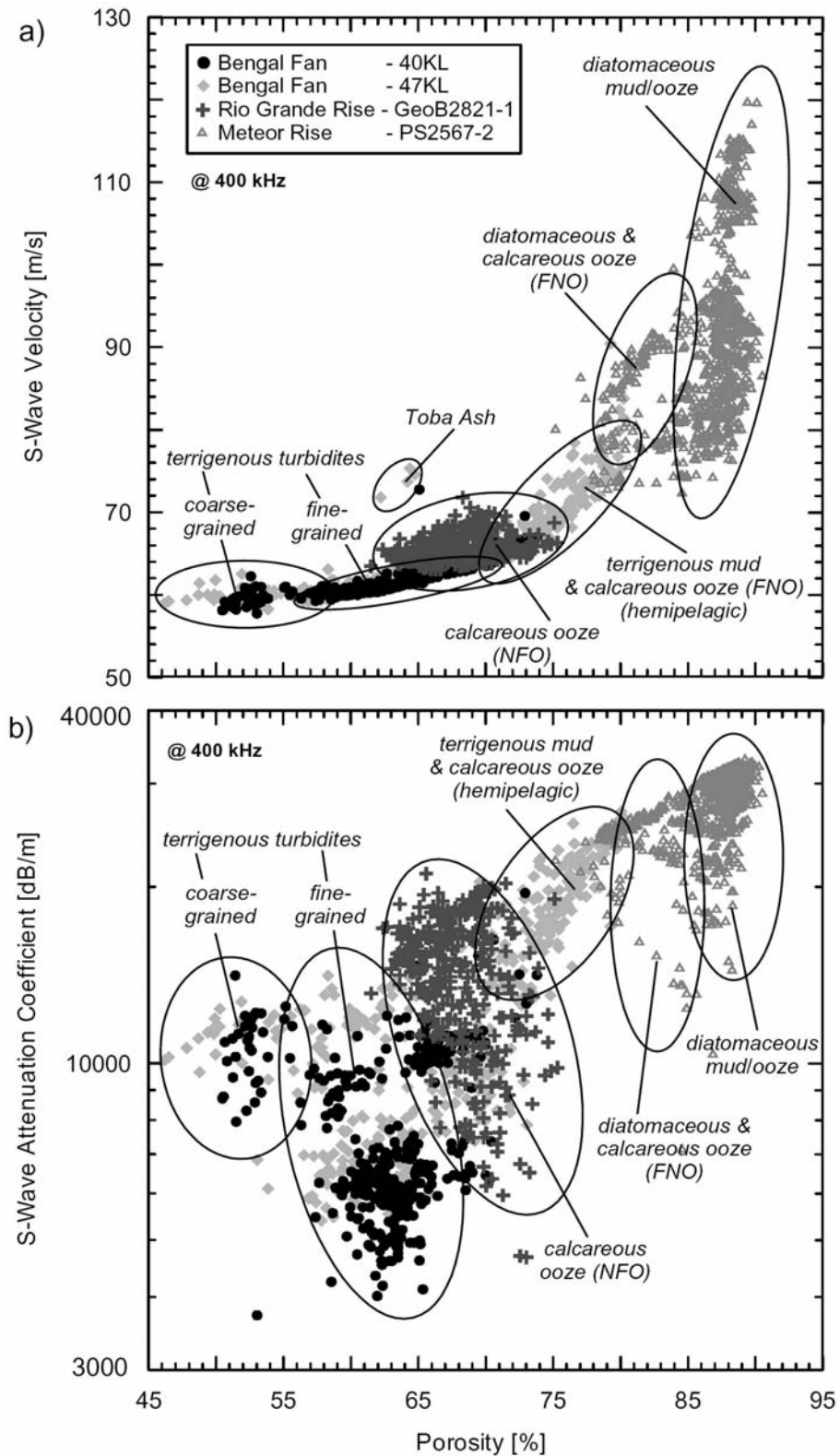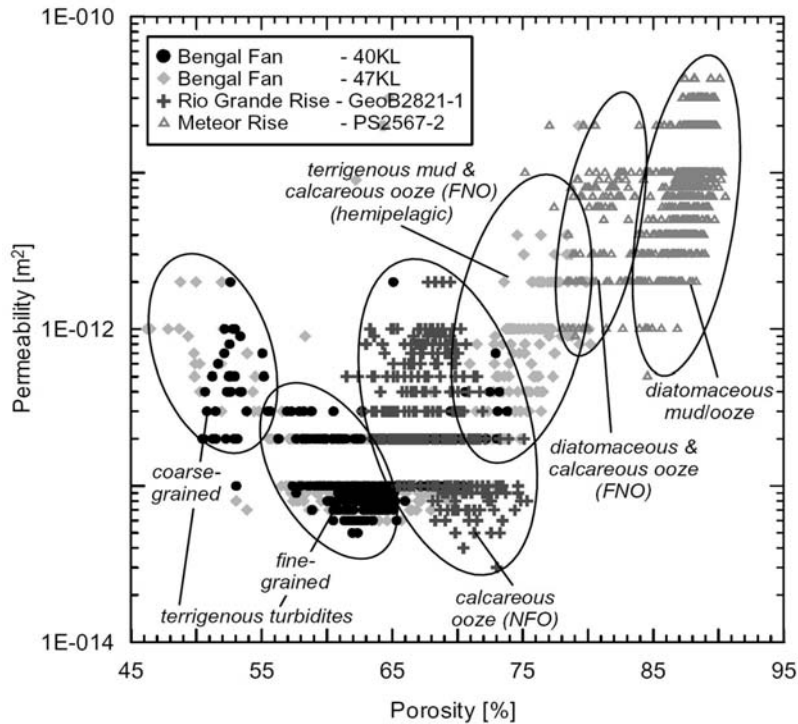
Fig. 2.20 (a) S-wave velocities and (b) attenuation coefficients (at 400 kHz) derived from least square inversion based on Biot-Stoll's theory versus porosities for the four sediment cores 40KL, 47KL, GeoB2821-1, and PS2567-2. NFO and FNO as in Figure 2.19. Modified after Breitzke (2000).
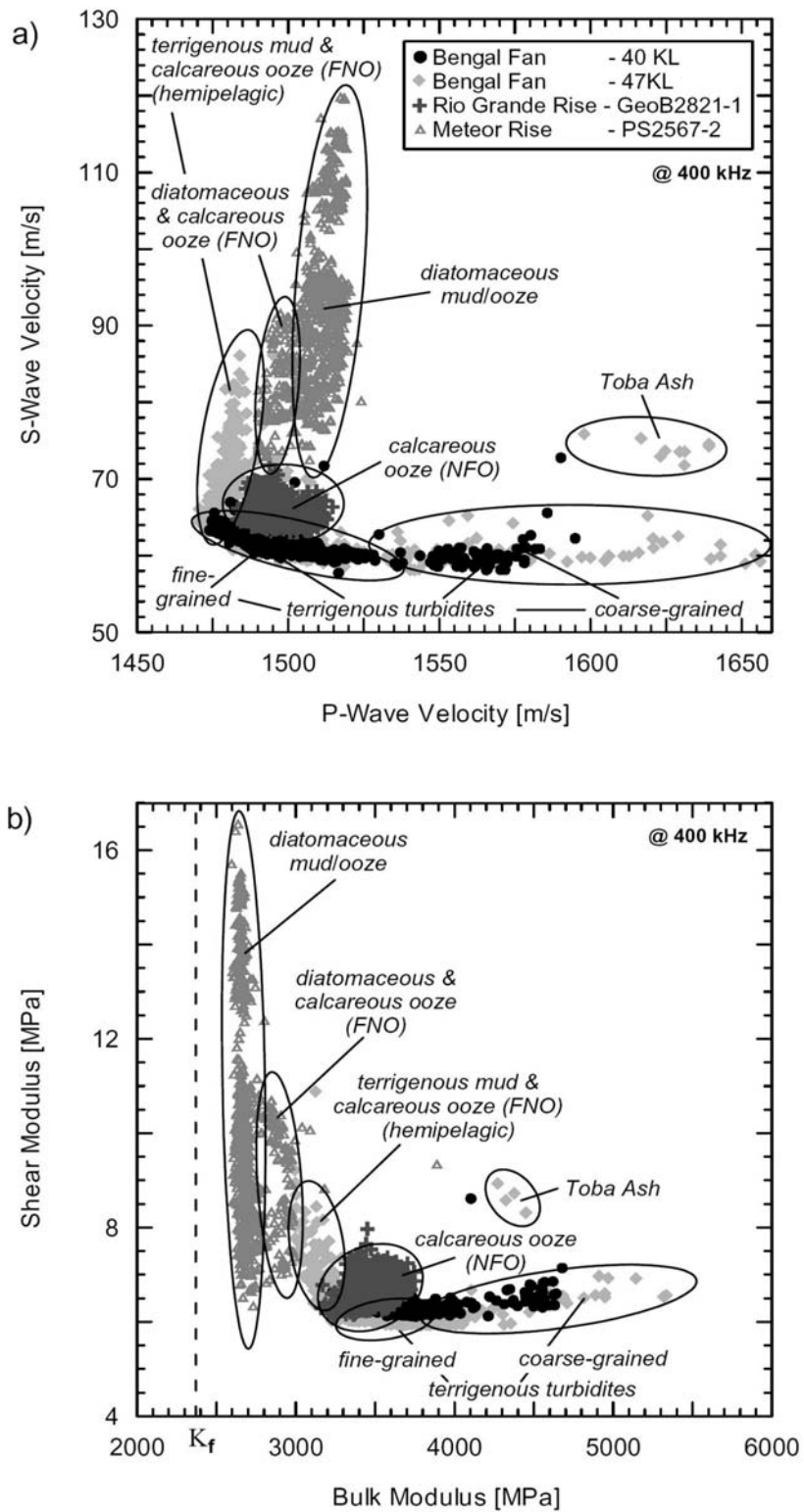
Fig. 2.21 (a) S-wave velocity versus P-wave velocity and (b) shear modulus versus bulk modulus derived from least square inversion based on Biot-Stoll's theory for the four sediment cores 40KL, 47KL, GeoB2821-1, and PS2567-2. The dotted line indicates an asymptote parallel to the shear modulus axis which crosses the value for the bulk modulus of seawater $K_f = 2370$ MPa on the bulk modulus axis. NFO and FNO as in Figure 2.19. Modified after Breitzke (2000).

Fig. 2.22 Permeabilities derived from least square inversion based on Biot-Stoll's theory versus porosities for the four sediment cores 40KL, 47KL, GeoB2821-1, and PS2567-2. The regular spacing of the permeability values is due to the increment (10 permeability values per decade) used for the optimization process in the inversion scheme. NFO and FNO as in Figure 2.19. Modified after Breitzke (2000).

multiples. Convolution with a source wavelet finally provides the synthetic seismogram. In practice, different time- and frequency domain methods exist for synthetic seismogram computations. For an overview, please refer to books an theoretical seismology (e.g. Aki and Richards, 2002). Here, we used a time domain method called 'state space approach' (Mendel et al. 1979).

Figure 2.24 compares the synthetic seismogram computed for core 47KL with the Parasound seismograms recorded at the coring site. The P-wave velocity and wet bulk density logs used as input parameters are displayed on the right-hand side, together with the attenuation coefficient log as grain size indicator, the carbonate content and an oxygen isotope ($\delta^{18}O$-) stratigraphy. An enlarged part of the gray shaded Parasound seismogram section is shown on the left-hand side. The comparison of synthetic and Parasound data indicates some core deformations. If the synthetic seismograms are leveled to the prominent reflection caused by the Toba Ash in 1.6 m depth about 95 cm sediment are missing in the overlying younger part of the core. Deeper reflec-

tions, particularly caused by the series of turbidites below 6 m depth, can easily be correlated between synthetic and Parasound seismograms, though single turbidite layers cannot be resolved due to their short spacing. Slight core stretching or shortening are obvious in this lower part of the core, too.

From the comparison of the gray shaded Parasound seismogram section and the wiggle traces on the left-hand side with the synthetic seismogram, core logs and stratigraphy on the right-hand side the following interpretation can be derived. The first prominent reflection below sea floor is caused by the Toba Ash layer deposited after the explosion of volcano Toba (Sumatra) 75,000 years ago. The underlying series of reflection horizons (about 4 m thickness) result from an interlayering of very fine-grained thin terrigenous turbidites and pelagic sediments. They are younger than about 240,000 years (oxygen isotope stage 7). At that time the channel was already inactive. The following transparent zone between 4.5 - 6.0 m depth indicates the transition to the time when the channel was active, more than
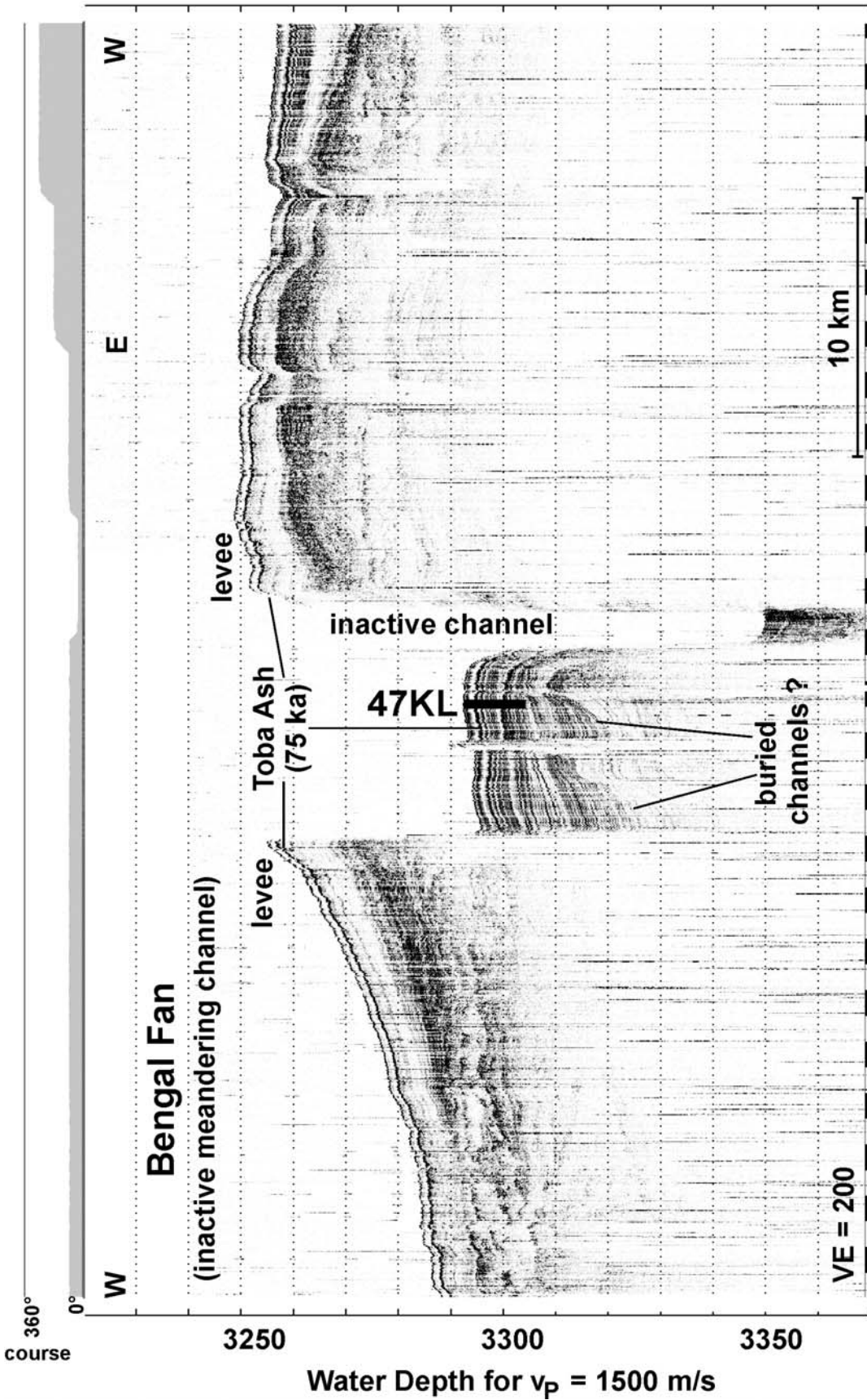
Fig. 2.23 Parasound seismogram section recorded across an inactive meandering channel in the Bengal Fan. The sediments of the terrace were sampled by piston core 47KL marked by the black bar. Vertical exaggeration (VE) of sedimentary structures is 200. The ship's course is displayed above the seismogram section. The terrace exhibits features which might be interpreted as old buried channels. Modified after Breitzke (1997).
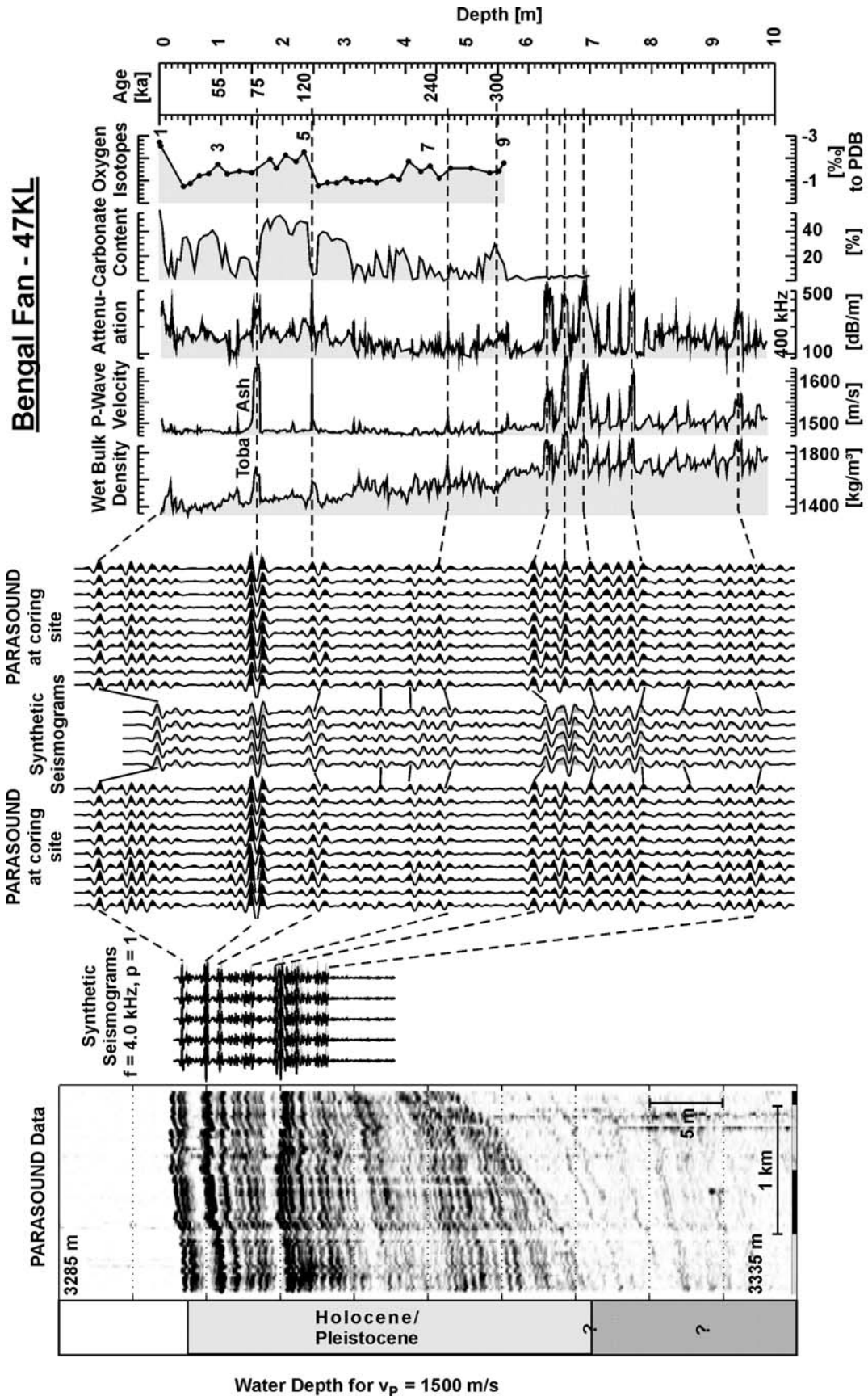
Fig. 2.24 Coring site of 47KL. *From left to right:* Enlarged part of the Parasound seismogram section recorded on approaching site 47KL. Comparison of synthetic seismograms computed on basis of P-wave velocity and wet bulk density measurements on 47KL with Parasound seismograms recorded at the coring site. Physical properties and age model of piston core 47KL. Wet bulk densities, carbonate content and oxygen isotope stratigraphy (*G. ruber pink*) are taken from (Kudrass 1994, 1996). Modified after Breitzke (1997).

300,000 years ago. Only terrigenous turbidites causing strong reflections below 6 m depth were deposited.

Transferred to the Parasound seismogram section in Figure 2.23 this interpretation means that the first prominent reflection horizon in the levees can also be attributed to the Toba Ash layer (75 ka). The following transparent zone indicates completely pelagic sediments deposited on the levees during the inactive time of the channel (< 240 ka). The suspension cloud was probably trapped between the channel walls so that only very thin, fine-grained terrigenous turbidites were deposited on the terrace but did not reach the levee crests. The high reflectivity part below the transparent zone in the levees is probably caused by terrigenous turbidites deposited here more than 300,000 years ago during the active time of the channel.

2.6.2   Narrow-Beam Parasound Echosounder Recordings

Finally, some examples of Parasound echosounder recordings from different terrigenous and biogenic provinces are presented to illustrate that characteristic sediment compositions can already be recognized from such remote sensing surveys prior to the sediment core retrieval.

The first example was recorded on the Rio Grande Rise in the western South Atlantic during RV Meteor cruise M29/2 (Bleil et al. 1994) and is typical for a calcareous environment (Fig. 2.25a). It is characterized by a strong sea bottom reflector caused by coarse-grained foraminiferal sands. Signal penetration is low and reaches only about 20 m.

In contrast, the second example from the Conrad Rise in the Antarctic Ocean, recorded during RV Polarstern cruise ANT XI/4 (Kuhn, pers. communication), displays a typical biogenic siliceous environment (Fig. 2.25b). The diatomaceous sediment coverage seems to be very transparent, and the Parasound signal penetrates to about 160 m depth. Reflection horizons are caused by calcareous foraminiferal and nanno-fossil layers deposited during a retreat of the Polar Frontal Zone during interglacial stages.

The third example recorded in the Weddell Sea/Antarctic Ocean during RV Polarstern cruise ANT XI/4 as well (Kuhn, pers. communication) indicates a deep sea environment with clay sediments (Fig. 2.25c). Signal penetration again is high (about 140 m), and reflection horizons are very

sharp and distinct. Zones with upward curved reflection horizons might possibly be indicators for pore fluid migrations.

The fourth example from the distal Bengal Fan (Hübscher et al. 1997) was recorded during RV Sonne cruise SO125 and displays terrigenous features and sediments (Fig. 2.25d). Active and older abandoned channel levee systems are characterized by a diffuse reflection pattern which indicates sediments of coarse-grained turbidites. Signal penetration in such environments is rather low and reaches about 30 - 40 m.

Acknowledgment

Appendix

A: Physical Properties of Sediment Grains and Sea Water

The density (ρ_g) and bulk modulus (K_g) of the sediment grains are the most important physical properties which characterize the sediment type - terrigenous, calcareous and siliceous - and composition. Additionally, they are required as input parameters for wave propagation modeling,
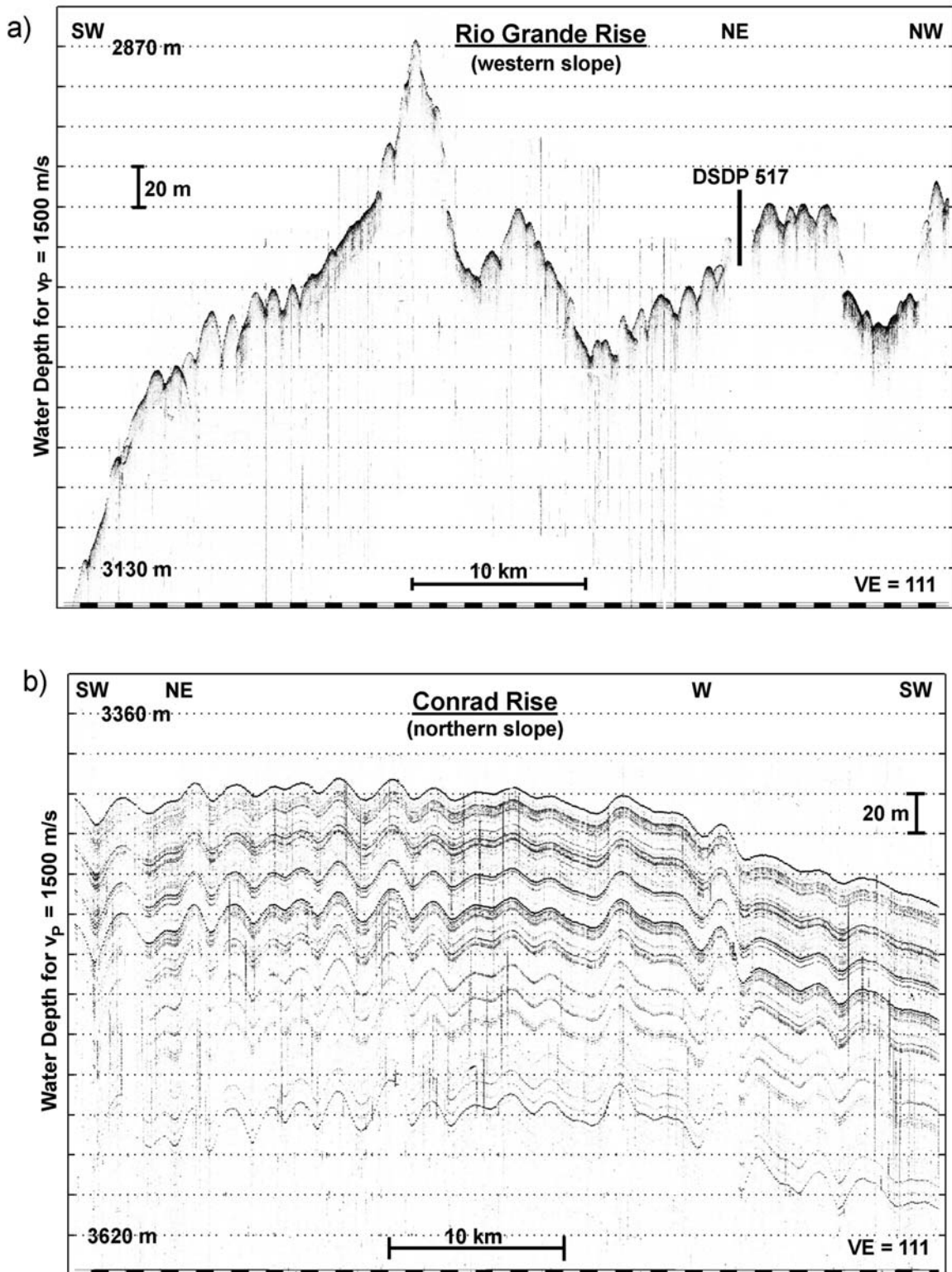
Fig. 2.25 a, b Parasound seismogram sections representing typical calcareous (Rio Grande Rise) and opal-rich diatomaceous (Conrad Rise) environments. Lengths and heights of both profiles amount to 50 km and 300 m, respectively. Vertical exaggeration (VE) is 111. The Parasound seismogram section from the Conrad Rise was kindly provided by G. Kuhn, Alfred-Wegener-Institute for Polar- and Marine Research, Bremerhaven, Germany and is an unpublished data set recorded during RV Polarstern cruise ANT IX/4. Modified after Breitzke (1997).

Fig. 2.25 c, d Parasound seismogram sections representing typical deep sea clay (Weddell Sea) and terrigenous sediments (Bengal Fan). Lengths and heights of both profiles amount to 50 km and 300 m, respectively. Vertical exaggeration (VE) is 111. The Parasound seismogram section from the Weddell Sea was kindly provided by G. Kuhn, Alfred-Wegener-Institute for Polar- and Marine Research, Bremerhaven, Germany and is an unpublished data set recorded during RV Polarstern cruise ANT IX/4. Modified after Breitzke (1997).
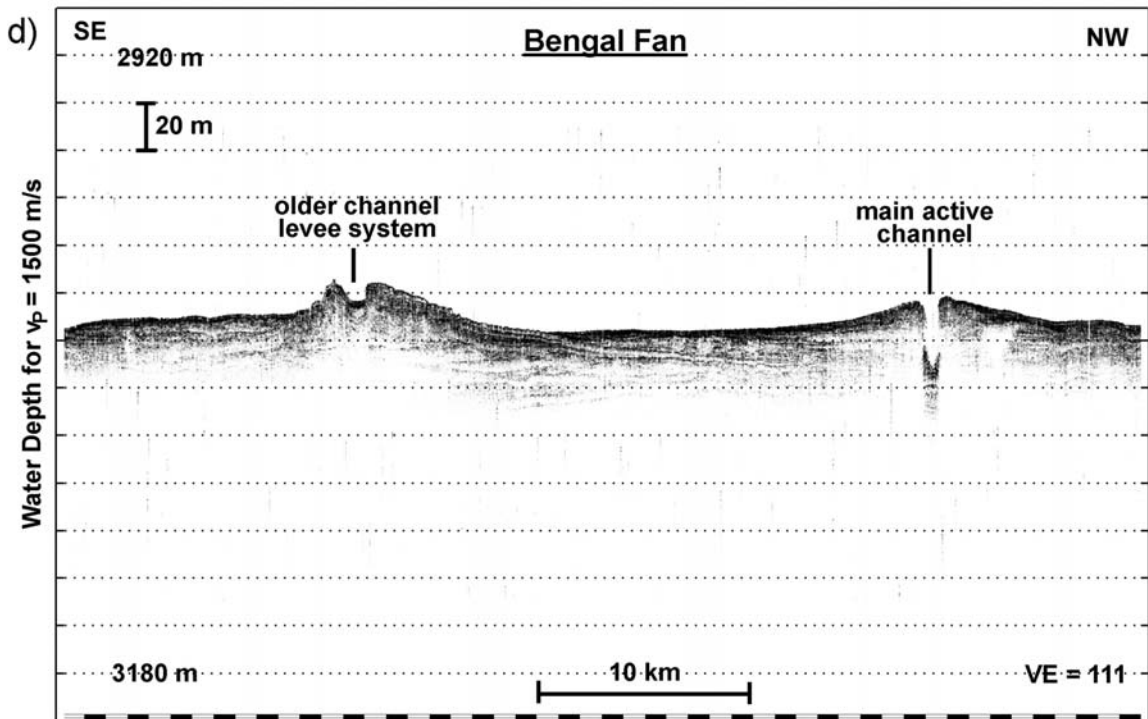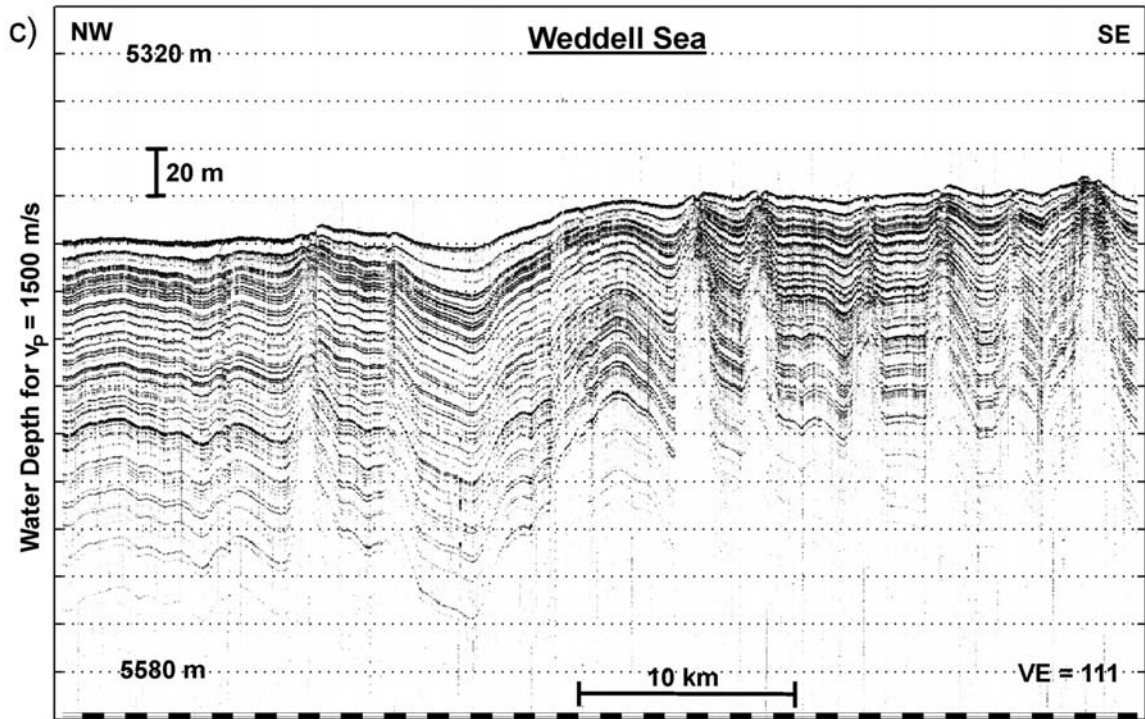
e.g. with Biot-Stoll's sediment model (Sect. 2.4.1). Table 2A-1 provides an overview on densities and bulk moduli of some typical sediment forming minerals.

Density (ρ_f), bulk modulus (K_f), viscosity (η), sound velocity (v_p), sound attenuation coefficient (α) and electrical resistivity (R_f) of sea water depend on salinity, temperature and pressure. Table 2A-2 summarizes their values at laboratory

conditions, i.e. 20°C temperature, 1 at pressure and 35‰ salinity.

B: Corrections to Laboratory and In Situ Conditions

Measurements of physical properties are usually carried out under laboratory conditions, i.e. room temperature (20°C) and atmospheric pressure (1 at).

Table 2A-1 Physical properties of sediment forming minerals, at laboratory conditions (20°C temperature, 1 at pressure). After [1]Wohlenberg (1982) and [2]Gebrande (1982).

Mineral	Density[1] ρ_g [g cm^{-3}]	Bulk Modulus[2] K_g [10^9 Pa]
terrigenous sediments		
quartz	2.649 - 2.697	37.6 - 38.1 (trigonal)
biotite	2.692 - 3.160	42.0 - 60.0
muscovite	2.770 - 2.880	43.0 - 62.0
hornblende	3.000 - 3.500	84.0 - 90.0
calcareous sediments		
calcite	2.699 - 2.882	70.0 - 76.0
siliceous sediments		
opal	2.060 - 2.300	no data

Table 2A-2 Physical properties of sea water, at laboratory conditions (20°C temperature, 1 at pressure, 35‰ salinity). After [1]Wille (1986) and [2]Siedler and Peters (1986).

Parameter	Value
sound velocity[1] v_P [m s^{-1}]	1521 m s^{-1}
sound attenuation coefficient[1] α [10^{-3} dB m^{-1}]	
4 kHz	~0.25
10 kHz	~0.80
100 kHz	~ 40
400 kHz	~ 120
1000 kHz	~ 300
density[2] ρ_f [g/cm^{-3}]	1.024
bulk modulus[2] K_f [10^9 Pa]	2.37
viscosity[2] η [10^{-3} Pa·s]	1.07
electrical resistivity[2] R_f [Ω·m]	0.21

In order to correct for slight temperature variations in the laboratory and to transfer laboratory measurements to in situ conditions, usually temperature and in situ corrections are applied. Temperature variations mainly affect the pore fluid. Corrections to in situ conditions should consider both the influence of reduced temperature and increased hydrostatic pressure at the sea floor.

Porosity and Wet Bulk Density

In standard sea water of 35‰ salinity density increases by maximum $0.3 \cdot 10^{-3}$ g cm^{-3} per °C (Siedler and Peters 1986), i.e. by less than 0.1% per °C. Hence, temperature corrections can usually be neglected.

Differences between laboratory and in-situ porosities are less than 0.001% (Hamilton 1971) and can thus be disregarded, too. Sea floor wet bulk densities are slightly higher than the corresponding laboratory values due to the hydrostatic pressure and the resulting higher density of the pore water. For Central Pacific sediments of 75 - 85% porosity Hamilton (1971) estimated a density increase of maximum 0.01 g cm^{-3} for water depths between about 500 - 3000 m and of maximum 0.02 g cm^{-3} for water depths between about 3000 - 6000 m. Thus, corrections to sea floor conditions are usually of minor importance, too. However, for cores of several hundred meter length the effect of an increasing lithostatic pressure has to be taken into account.

Electrical Resistivity

If porosities and wet bulk densities are determined by galvanic resistivity measurements (Sect. 2.2.3) varying sediment temperatures are considered by computation of the formation factor (F) (see Eq. 2.12). While the resistivity (R_s) of the sediment is determined by the small hand-held probe (cf. Sect. 2.2.3) the resistivity (R_f) of the pore fluid is derived from a calibration curve which describes the temperature (T) - conductivity (c) relation by a fourth power law (Siedler and Peters 1986)

$$R_f^{-1} = c_o + c_1 T + c_2 T^2 + c_3 T^3 + c_4 T^4 \qquad (2.22)$$

The coefficients (c_0) to (c_4) depend on the geometry of the probe and are determined by a least square fit to the calibration measurements in standard sea water.

P-wave velocity and attenuation

Bell and Shirley (1980) demonstrated that the P-wave velocity of marine sediments increases almost linearly by about 3 m s^{-1} per °C while the attenuation is independent of sediment temperature, similar to the temperature dependence of sound velocity and attenuation in sea water. Hence, to correct laboratory P-wave velocity measurements to a reference temperature of 20°C Schultheiss and McPhail's (1989) equation

$$v_{20} = v_T + 3 \cdot (20 - T) \qquad (2.23)$$

can be applied, with (v_{20}) = P-wave velocity at 20°C (in m s^{-1}), (T) = sediment temperature (in °C) and (v_T) = P-wave velocity measured at temperature (T) (in m s^{-1}).

To correct laboratory P-wave velocity measurements to in situ conditions a modified time-average equation (Wyllie et al. 1956) can be used (Shipboard Scientific Party 1995)

$$\frac{1}{v_{insitu}} = \frac{1}{v_{lab}} + \phi \cdot \left(\frac{1}{c_{insitu}} - \frac{1}{c_{lab}} \right) \qquad (2.24)$$

(v_{lab}) and ($v_{in\text{-}situ}$) are the measured laboratory (20°C, 1 at) and the corrected in situ P-wave velocities, (c_{lab}) and ($c_{in\text{-}situ}$) the sound velocity in sea water at laboratory and in situ conditions and (ϕ) the porosity. If laboratory and sea floor pressure, temperature and salinity are known from tables or CTD measurements (c_{lab}) and ($c_{in\text{-}situ}$) can be computed according to Wilson's (1960) equation

$$c = 1449.14 + c_T + c_P + c_S + c_{STP} \qquad (2.25)$$

(c_T), (c_P), (c_S) are higher order polynomials which describe the influence of temperature (T), pressure (P) and salinity (S) on sound velocity. (c_{STP}) depends on all three parameters. Complete expressions for (c_T), (c_P), (c_S), (c_{STP}) can be found in Wilson (1960). For T = 20°C, P = 1 at and S = 0.035 Wilson's equation results in a sound velocity of 1521 m s^{-1}.

2.7 Problems

Problem 1

What is the difference between bulk parameters and acoustic/elastic parameters concerning the distribution of pore fluid and sediment grains ?

Problem 2

Which direct and which indirect methods do you know to determine the porosity and wet bulk density of marine sediment, which of both parameters is primarily determined by each method, and how can porosity values be converted to density values and vice versa ?

Problem 3

Assume that you have recovered a sediment core in the Antarctic Ocean close to the Polar Frontal Zone. The core is composed of an interlayering of calcareous and siliceous sediments. You would like to determine the downcore porosity and wet bulk density logs by electrical resitivity measurements. What do you have to consider during conversion of porosities to wet bulk densities ?

Problem 4

Which sediment property mainly influences the ultrasonic acoustic wave propagation (50 - 500 kHz), and how affects it the P-wave velocity and attenuation in terrigenous and calcareous sediments ?

Problem 5

Which parameter determines the amplitude or strength of reflection horizons during sediment echosounding, and which are the two physical properties that contribute to it ?

References

Aki K., Richards P.G., 2002. Quantitative Seismology. University Science Books, 700 pp

Archie G.E., 1942. The electrical resistivity log as an aid in determining some reservoir characteristics. Transactions of the American Institute of Mineralogical, Metalurgical and Petrological Engineering 146: 54-62

Barker P.F., Kennett J.P. et al., 1990. Proceedings of the Ocean Drilling Program, Scientific Results 113, College Station, TX (Ocean Drilling Program), 1033 pp

Bell D.W., Shirley D.J., 1980. Temperature variation of the acoustical properties of laboratory sediments. Journal of the Acoustical Society of America 68: 227-231

Bergmann U., 1996. Interpretation of digital Parasound echosounder records of the eastern Arctic Ocean on the basis of sediment physical properties. Rep. on Polar Research, Alfred-Wegener Institute for Polar and Marine Research, Bremerhaven 183: 164 pp

Berryman J.G., 1980. Confirmation of Biot's theory. Applied Physics Letters 37: 382-384

Biot M.A., 1956a. Theory of propagation of elastic waves in a fluid-saturated porous solid. II. Higher frequency range. Journal of the Acoustical Society of America 28: 179-191

Biot M.A., 1956b. Theory of wave propagation of elastic waves in a fluid-saturated porous solid. I. Low-frequency range. Journal of the Acoustical Society of America 28: 168-178

Bleil U. et al., 1994. Report and preliminary results of Meteor cruise M29/2 Montevideo - Rio de Janeiro, 15.07. - 08.08.1994. Ber. FB Geow. Univ. Bremen 59: 153 pp

Blum P., 1997. Physical properties handbook: a guide to the shipboard measurement of physical properties of deep-sea cores. Technical Note 26, Ocean Drilling Program, College Station, Texas

Bodwadkar S.V., Reis J.C., 1994. Porosity measurements of core samples using gamma-ray attenuation. Nuclear Geophysics 8: 61-78

Boyce R.E., 1968. Electrical resistivity of modern marine sediments from the Bering Sea. Journal of Geophysical Research 73: 4759-4766

Boyce R.E., 1973. Appendix I. Physical properties - Methods. In: Edgar NT, Sanders JB et al (eds) Initial Reports of the Deep Sea Drilling Project 15, Washington, US Government Printing Office, pp 1115-1127

Boyce R.E., 1976. Definitions and laboratory techniques of compressional sound velocity parameters and wet-water content, wet-bulk density, and porosity parameters by gravity and gamma ray attenuation techniques. In: Schlanger S.O., Jackson E.D. et al (eds) Initial Reports of the Deep Sea Drilling Project 33, Washington, US Government Printing Office, pp 931-958

Breitzke M., Spieß V., 1993. An automated full waveform logging system for high-resolution P-wave profiles in marine sediments. Marine Geophysical Researches 15: 297-321

Breitzke M., Grobe H., Kuhn G., Müller P., 1996. Full waveform ultrasonic transmission seismograms - a fast new method for the determination of physical and sedimentological parameters in marine sediment cores. Journal of Geophysical Research 101: 22123-22141

Breitzke M., 1997. Elastische Wellenausbreitung in marinen Sedimenten - Neue Entwicklungen der Ultraschall Sedimentphysik und Sedimentechographie. Ber. FB Geo Univ. Bremen 104: 298 pp

Breitzke M., 2000. Acoustic and elastic characterization of marine sediments by analysis, modeling, and inversion of ultrasonic P wave transmission seismograms, Journal of Geophysical Research 105: 21411-21430

Bryant W.R., Hottman W., Trabant P., 1975. Permeability of unconsolidated and consolidated marine sediments, Gulf of Mexico. Marine Geotechnology 1: 1-14

Carman P.C., 1956. Flow of gases through porous media. Butterworths Scientific Publications, London, 182 pp

Chelkowski A., 1980. Dielectric Physics. Elsevier, Amsterdam, 396 pp

Childress J.J., Mickel T.J., 1980. A motion compensated shipboard precision balance system. Deep Sea Research 27A: 965-970

Constable C., Parker R., 1991. Deconvolution of log-core paleomagnetic measurements - spline therapy for the linear problem. Geophysical Journal International 104: 453-468

Courtney R.C., Mayer L.A., 1993. Acoustic properties of fine-grained sediments from Emerald Basin: toward an inversion for physical properties using the Biot-Stoll model. Journal of the Acoustical Society of America 93: 3193-3200

Dobeneneck v.T., Schmieder F., 1999. Using rock magnetic proxy records for orbital tuning and extended time series analyses into the super- and sub-Milankovitch bands. In: Fischer G and Wefer G (eds) Use of proxies in paleoceanography: examples from the South Atlantic. Springer Verlag Berlin, pp 601 - 633.

Ellis D.V., 1987. Well logging for earth scientists. Elsevier, Amsterdam, 532 pp

Fisher A.T., Fischer K., Lavoie D., Langseth M., Xu J., 1994. Geotechnical and hydrogeological properties of sediments from Middle Valley, northern Juan de Fuca Ridge. In: Mottle M.J., Davis E., Fisher A.T., Slack J.F. (eds) Proceedings of the Ocean Drilling Program, Scientific Results 139, College Station, TX (Ocean Drilling Program), pp 627-647

Gassmann F., 1951. Über die Elastizität poröser Medien. Vierteljahresschrift der Naturforschenden Gesellschaft in Zürich 96: 1-23

Gealy E.L., 1971. Saturated bulk density, grain density and porosity of sediment cores from western equatorial Pacific: Leg 7, Glomar Challenger. In: Winterer E.L. et al. (eds) Initial Reports of the Deep Sea Drilling Project 7, Washington, pp 1081-1104

Gebrande H., 1982. Elastic wave velocities and constants of elasticity at normal conditions. In: Hellwege K.H. (ed) Landolt-Börnstein. Numerical Data and Functional Relationships in Science and Technology. Group V: Geophysics and Space Research 1, Physical Properties of Rocks, Subvolume b, Springer Verlag, Berlin, pp 8-35

Gerland S., 1993. Non-destructive high resolution density measurements on marine sediments. Rep. on Polar Research, Alfred-Wegener Institute for Polar and Marine Research, Bremerhaven 123: 130 pp

Gerland S., Richter M., Villinger H., Kuhn G., 1993. Non-destructive porosity determination of Antarctic marine sediments derived from resistivity measurements with the inductive method. Marine Geophysical Researches 15: 201-218

Gerland S., Villinger H., 1995. Nondestructive density determination on marine sediment cores from gamma-ray attenuation measurements. Geo-Marine Letters 15: 111-118

Gunn D.E., Best A.I., 1998. A new automated nondestructive system for high resolution multi-sensor logging of open sediment cores. Geo-Marine Letters 18: 70-77

Hamilton E.L., 1971. Prediction of in situ acoustic and elastic properties of marine sediments. Geophysics 36: 266-284

Hovem J.M., Ingram G.D., 1979. Viscous attenuation of sound in saturated sand. Journal of the Acoustical Society of America 66: 1807-1812

Hovem J.M., 1980. Viscous attenuation of sound in suspensions and high-porosity marine sediments. Journal of the Acoustical Society of America 67: 1559-1563

Hübscher C., Spieß V., Breitzke M., Weber M.E., 1997. The youngest channel-levee system of the Bengal Fan: results from digital echosounder data. Marine Geology 141: 125 - 145

Jackson P.D., Taylor-Smith D., Stanford P.N., 1978. Resistivity-porosity-particle shape relationships for marine sands. Geophysics 43: 1250-1268

Jannsen D., Voss J., Theilen F., 1985. Comparison of methods to determine Q in shallow marine sediments from vertical seismograms. Geophysical Prospecting 33: 479-497

Lambe T.W., Whitman R.V., 1969. Soil mechanics. John Wiley and Sons Inc, New York, 553 pp

Lovell M.A., 1985. Thermal conductivity and permeability assessment by electrical resistivity measurements in marine sediments. Marine Geotechnology 6: 205-240

MacKillop A.K., Moran K., Jarret K., Farrell J., Murray D., 1995. Consolidation properties of equatorial Pacific Ocean sediments and their relationship to stress history and offsets in the Leg 138 composite depth sections. In: Pisias N.G., Mayer L.A., Janecek T.R., Palmer-Julson A., van Andel T.H. (eds) Proceedings of the Ocean Drilling Program, Scientific Results 138, College Station, TX (Ocean Drilling Program), pp 357-369

Mazullo J.M., Meyer A., Kidd R.B., 1988. New sediment classification scheme for the Ocean Drilling Program. In: Mazullo JM, Graham AG (eds) Handbook for Shipboard Sedimentologists, Technical Note 8, Ocean Drilling Program, College Station, Texas, pp 45 - 67

Mendel J.M., Nahi N.E., Chan M., 1979. Synthetic seismograms using the state space approach. Geophysics 44: 880-895

O'Connell S.B., 1990. Variations in upper cretaceous and Cenozoic calcium carbonate percentages, Maud Rise, Weddell Sea, Antarctica. In: Barker P.F., Kennett J.P. et al. (eds) Proceedings of the Ocean Drilling Program, Scientific Results 113, College Station, TX (Ocean Program), pp 971-984

Ogushwitz P.R., 1985. Applicability of the Biot theory. II. Suspensions. Journal of the Acoustical Society of America 77: 441-452

Olsen H.W., Nichols R.W., Rice T.C., 1985. Low gradient permeability measurements in a triaxial system. Geotechnique 35: 145-157

Plona T.J., 1980. Oberservation of a second bulk com-

pressional wave in a porous medium at ultrasonic frequencies. Applied Physics Letters 36: 159-261

Ruffet C., Gueguen Y., Darot M., 1991. Complex conductivity measurements and fractal nature of porosity. Geophysics 56: 758-768

Schopper J.R., 1982. Permeability of rocks. In: Hellwege KH (ed) Landolt-Börnstein. Numerical Data and Functional Relationships in Science and Technology, Group V: Geophysics and Space Research 1, Physical Properties of Rocks, Subvolume a, Berlin, Springer Verlag, Berlin, pp 278-303

Schön J.H., 1996. Physical Properties of Rocks - Fundamentals and Principles of Petrophysics. Handbook of Geophysical Exploration 18, Section I, Seismic Exploration. Pergamon Press, Oxford, 583 pp

Schultheiss P.J., McPhail S.D., 1989. An automated P-wave logger for recording fine-scale compressional wave velocity structures in sediments. In: Ruddiman W, Sarnthein M et al (eds), Proceedings of the Ocean Drilling Program, Scientific Results 108, College Station TX (Ocean Drilling Program), pp 407-413

Sen P.N., Scala C., Cohen M.H., 1981. A self-similar model from sedimentary rocks with application to dielectric constant of fused glass beads. Geophysics 46: 781-795

Sheng P., 1991. Consistent modeling of electrical and elastic properties of sedimentary rocks. Geophysics 56, 1236-1243

Shipboard Scientific Party, 1995. Explanatory Notes. In: Curry W.B., Shackleton N.J., Richter C. et al. (eds), Proceedings of the Ocean Drilling Program, Initial Reports 154, College Station TX (Ocean Drilling Program), pp 11-38

Siedler G., Peters H., 1986. Physical properties (general) of sea water. In: Hellwege K.H., Madelung O. (eds) Landolt-Börnstein. Numerical Data and Functional Relationships in Science and Technology. Group V: Geophysics and Space Research 3, Oceanography, Subvolume a, Springer Verlag, Berlin, pp 233-264

Spieß V., 1993. Digitale Sedimentechographie - Neue Wege zu einer hochauflösenden Akustostratigraphie. Ber. FB Geo Univ. Bremen 35: 199 pp

Stoll R.D., 1974. Acoustic waves in saturated sediments. In: Hampton L. (ed) Physics of sound in marine sediments. Plenum Press, New York, pp 19-39

Stoll R.D., 1977. Acoustic waves in ocean sediments. Geophysics 42: 715-725

Stoll R.D., 1989. Sediment Acoustics. Springer Verlag, Berlin, 149 pp

Taner M.T., Koehler F., Sheriff R.E., 1979. Complex seismic trace analysis. Geophysics 44: 1041 - 1063

Tonn R., 1989. Comparison of seven methods for the computation of Q. Physics of the Earth and Planetary Interiors 55: 259-268

Tonn R., 1991. The determination of the seismic quality factor Q from VSP data: a comparison of different computational methods. Geophysical Prospecting 39: 1-27

Waxman M.H., Smits L.J.M., 1968. Electrical conductivities in oil bearing shaly sandstones. Society of Petroleum Engineering 8: 107-122

Weaver, P.P.E., Schultheiss P.J., 1990. Current methods for obtaining, logging and splitting marine sediment cores. Marine Geophysical Researches 12: 85-100

Weber M.E., Niessen F., Kuhn G., Wiedicke M., 1997. Calibration and application of marine sedimentary physical properties using a multi-sensor core logger. Marine Geology 136: 151-172

Weeks R., Laj C., Endignoux L., Fuller M., Roberts A., Manganne R., Blanchard E., Goree W., 1993. Improvements in long-core measurement techniques: applications in paleomagnetism and paleoceanography. Geophysical Journal International 114: 651-662

Whitmarsh R.B., 1971. Precise sediment density determination by gamma-ray attenuation alone, Journal of Sedimentary Petrology 41: 882-883

Wille P., 1986. Acoustical properties of the ocean. In: Hellwege KH, Madelung O (eds) Landolt-Börnstein. Numerical Data and Functional Relationships in Science and Technology. Group V: Geophysics and Space Research 3, Oceanography, Subvolume a, Springer Verlag, Berlin, pp 265-382

Wilson W.D., 1960. Speed of sound in sea water as a function of temperature, pressure and salinity. Journal of the Acoustical Society of America 32: 641-644

Wohlenberg J., 1982. Density of minerals. In: Hellwege K.H. (ed) Landolt-Börnstein. Numerical Data and Functional Relationships in Science and Technology. Group V: Geophysics and Space Research 1, Physical Properties of Rocks, Subvolume a, Springer Verlag, Berlin, pp 66-113

Wood A.B., 1946. A textbook of sound. G Bell and Sons Ltd, London, 578 pp

Wyllie M.R., Gregory A.R., Gardner L.W., 1956. Elastic wave velocities in heterogeneous and porous media. Geophysics 21: 41-70